16th June 2020

Dear Editor,

Thank you for your helpful comments on our manuscript entitled “Characteristics of earthquake ruptures and dynamic off-fault deformation on propagating faults” [Paper se-2020-16]. We are grateful for the constructive and thoughtful comments made by the reviewers. We have addressed their questions, which are quoted below in blue. Text in red indicates text added to the new version of the manuscript. We also provide a PDF version of the revised manuscript in which we highlighted the changes in red (deleted) and blue (added). All line numbers in the letter below refer to the tracked-changes document. We hope that our revised manuscript has clarified the questions raised by the reviewers and made the paper stronger.

Best regards,
Simon Preuss (on behalf of all co-authors)

Reviewer 1 - Michele Cooke

A. The assumption of lateral propagation of strike-slip faults does not consider how crustal faults might form by the upward propagation and/or linkage of early fault segments. Experiments of strike-slip fault evolution show upward propagation with the formation of an early set of echelon faults that link to form a through-going strike-slip fault (e.g., Tchalenko, 1970; Hatem et al., JSG 2017). We don’t have reason to believe that crustal strike-slip faults would initiate differently from experiment observations. The text uses results of Perrin et al. (2016) that faults are most mature along their centers to justify lateral propagation. Lateral variation in fault maturity don’t preclude early upward propagation that would produce echelon segments that may link earlier along some portions of the fault than others. Unlike the quasi-2D simulations in this paper, the base of 3D laboratory experiments distributes shear within the suprajacent material in a manner analogous to crustal systems where mid crustal deformation drives upper crustal faulting. I’m not saying that the investigation of lateral propagation of strike-slip faults within this paper is unreasonable. This is a great first step towards understanding the complex evolution of strike-slip faults but may be only part of the story. To strengthen the implications of the paper, the introduction and discussion of the manuscript should include consideration of the 3D context of these strike-slip faults. How might the findings differ if strike-slip faults initiate with upward propagation followed by linkage?
We thank the reviewer for this thoughtful comment and for pointing out differences between 2D and 3D experiments. Indeed, our 2D (map view) and 2.5D simulations cannot model upward propagation of fault segments. However, there are other scenarios for fault strike-slip formation that are mechanically viable, such as those demonstrated in our paper and

supported by field observations and other lab experiments. Both scenarios are not exclusive: it is very possible that the initiation of a fault is driven from below by the process the reviewer describes, but, as shown here and elsewhere, the subsequent lateral growth does not need to be driven from below.
We have followed a common practice in 2D numerical modeling of fault growth/branching or rupture propagation in strike-slip faults to simulate map view experiments (e.g. Kame et al., 1999; Poliakov et al., 2002; Rice et al., 2005; Meyer et al., 2017; Herrendörfer et al., 2018; Preuss et al., 2019). With our approach we are focusing on a very important part of the problem: the lateral growth stage.
To strengthen and clarify the scope of the paper we add the following to the introduction (line 31) :
Analogue experiments have shown that strike-slip faults can initiate by upward propagation and linkage of an early set of echelon faults to form a through-going fault (e.g. Tchalenko, 1970; Hatem et al., 2017). Further growth towards a through-going strike-slip fault generally occurs due to lateral propagation and the structural fault complexity usually increases towards the younger portions at the fault tip (Perrin et al., 2016a; Cappa et al., 2014).

And we add to the existing text (black italic) in the discussion section (line 688) :
This approximation does not actually account for the third dimension and neglects parameter variations with depth as well as a possible change of the fault dip angle with depth. In this study faults are always vertical in a plane-strain sense, cutting through the entire upper crustal layer. This implies that faults in our models can not initiate at depth and link from an early set of echelon faults that propagate upwards as shown by analogue experiments. *Further, the simulations exclude a temperature-dependent rheology that would imply rheology changes with depth.*

B. The conclusions that the strike-slip faults grow predominantly in the aseismic period of the earthquake cycle is based on the assessment that the rate weakening results, with their fast coseismic growth, are unreasonable.
We emphasize that all four reference models have predominantly aseismically growing faults. This was stated at various points in the old version of the manuscript already. The longest seismically grown fault segment in the rate weakening model measures 12.3 km (line 313) and the rest of the newly formed fault (i.e. ~30 km for fault RW2) was produced aseismically. Moreover, the rate weakening model does not have faster and more coseismic growth than the other models. We add that the rate weakening results are not per se considered unreasonable. Our results in section 3.1 show that a bulk rheology with constant rate-sensitivity (including the rate weakening model) favors a faster fault growth of up to 77 km/yr in contrast to more realistic fault growth rates of ~1.8 km/yr in model RT.
To clarify our findings we add to line 483 (beginning of discussion):
Our results suggest that all four reference models have predominantly aseismically growing faults. A bulk rheology with constant rate-sensitivity favors a faster fault growth. In contrast, the heterogeneities introduced by a weakening of the RSF parameters L and b slow down the

faulting process due to the absorption of energy by the weakening mechanism. As a consequence, the faults in the model RT that transition from rate-strengthening to rate-weakening can extend in alternating seismic and aseismic growth periods. Only if the region ahead of the fault tip has experienced distinct plastic strain and L and b are altered to create a rate-weakening fault earthquakes can propagate on there. Otherwise, dynamic rupturing is hindered in the intact bulk, where L is still high and b is still low and rate-strengthening, respectively. This contrast of large L and low b in the bulk rock results in intermittent seismic and aseismic growth sequences. We think this behaviour reflects the natural growth of crustal faults better than constant values of L and b, which lead to rapid fault propagation after singular earthquakes.
Furthermore, evolution of L and b with strain was observed in laboratory studies (e.g. Beeler et al., 1996; Scuderi et al., 2017; Marone and Kilgore, 1993).
The differences between the two end-member bulk rheologies have major implications on the dynamics and geometry of fault evolution, which are discussed in this section.

We furthermore add to line 553:
However, in general fault growth predominantly occurs through aseismic deformation in all four reference models, independent of the type of bulk rheological behaviour. That is because a seismic rupture only reaches the current fault tip if this part of the fault is already highly localized. This is solely the case in the first earthquake when the entire fault trace coincides with the predefined, weak, mature fault.

We furthermore add to line 260:
The models with constant rate-sensitivity (models RS, RN, and RW) have fast fault growth rates of up to 77 km/yr that are much faster than in model RT. Despite this major difference, all reference models have in common that fault growth during the earthquakes contributes only a small portion to the total formed fault length FL (Fig. [3b]).

We do have evidence that faults can link during earthquake rupture along previously unmapped segments. This process of quick coseismic linkage could look a lot like the results of the rate weakening models that propagate towards the edges of the model. If the models had a second fault segment, perhaps the rate weakening models would showing linkage of the segments in a very reasonable way. For this reason, perhaps the rate weakening rheology may be overlooked should not be considered completely unreasonable.
We agree that fault linkage can occur during earthquake rupture along previously unmapped segments. We did show this in Figure 9 for model HPT. Adding to that we explained in the previous comment that we do not per se consider the rate weakening rheology as unreasonable.
We are currently running models of a natural earthquake example in which we predefine several unlinked segments that are supposed to link on the long-term (Preuss et al., 2020, EGU General Assembly 2020 presentation: link). However, fault linkage is a complex

process that needs further investigation and is not among the main aspects of this paper, which is already long. We refer to the last two sentences of our manuscript:
With our work we provide the basis for simulations and analyses of complex evolving fault networks subject to long-term and short-term dynamics. The approach we presented has potential to be applied to a more realistic fault map in a future study.

C. This question is related to the comment of B. Rate neutral and rate weakening are rheologies that we expect in the crust. In this study, they are excluded because the models do not produce more than one earthquake. What model parameters could be altered (for example, in a future study) to get more than one earthquake cycle for the rate neutral and rate weakening models?
We are not sure if rate neutral and rate weakening are the most realistic rheologies we can expect in the crust. Laboratory observations show that RSF parameters *(a-b)* and *L* weaken with plastic strain (Beeler et al., 1996; Scuderi et al., 2017; Marone and Kilgore, 1993). This behavior suggests that a crustal bulk rheology with no rate-sensitivity (like constant rate-neutral or constant rate-weakening) is less likely. We conducted up to ~1000 experiments with different parameter setups but were unable to get to more than one earthquake or distinctly slower fault growth rates in any of those models with no rate-sensitivity.
In contrast a rate sensitivity as observed in laboratory studies is incorporated in model RT, which produces the most realistic fault growth rates and earthquake sequences rather than single earthquakes. Thus, we consider model RT the most realistic model and the rate-transitioning rheology the most likely crustal behaviour.
In a future study we suggest to test the following to get more than one earthquake cycle for the rate neutral and rate weakening models:

- Substantially larger model box with mesh refinement close to the fault
- Strongly misaligned initital fault
- Higher value of background pressure
- Higher initial bulk state variable
- Higher cohesion potentially in combination with strain weakening of cohesion

D. Some parameters seem a bit outside of expected crustal ranges. The width of the plastic yielding fan seems large.
We emphasize that observations distinguish between outer and inner damage zones. The "outer damage zone" (Perrin et al., 2016) is much bigger than the "inner damage zone" (Savage and Brodsky, 2011). In our study we furthermore find that the initial orientation of the fault and various parameter(-combinations) alter the width of the plastic yielding fan severely:
In section 3.3 and particularly in Figure 8 we show that the width of the plastic yielding fan depends on the initial orientation of the fault in the surrounding stress field. The large fan width results from the misorientation of the predefined fault. Thus the initial fault orientation

relative to the regional stress is a crucial parameter. A corollary is the possibility to distinguish between optimally oriented and severely misoriented faults by assessing the extent of coseismic off-fault damage.
In section 4.4 we comment on this particularity of our findings. For example we write in line 582:
Our findings regarding the time-dependent optimality of the fault angle have implications for nature and for future dynamic rupture modeling studies. Active fault strands in nature that are surrounded by severe localized or diffuse damage zones, possibly extending far into the host rock, are strongly misaligned with the interseismic far-field stress field. This misalignment may be increased dynamically during seismic rupturing. This means that individual fault traces may reflect the local geology, structure or stress state rather than the prevailing far-field, long-term stress field and this effect would vary from segment to segment randomizing the fault pattern (Moore and Byerlee, 1989). This explains the complex nature of inter-branched crustal fault systems.

We add the following to the new version of the manuscript (line 669):
The width of the plastic fan in our models is larger than that seen in observations from Savage and Brodsky (2011). This difference is related to the non-optimally oriented fault of the reference model, which was discussed in section 4.4 and which is compared to an optimally oriented fault with a significantly lower width of the plastic yielding fan in figure 8. Furthermore, the plane strain assumption in our 2.5-D model assumes a constant thickness of the seismogenic fault with depth-constant rate-weakening behavior, which favours a larger width of the plastic yielding fan generated during earthquakes if it is compared to a natural fault which typically has alternating rate-weakening and rate-strengthening patches. Additionally, in our model the width of the fan is controlled by several parameters, of which the thickness of the elastic layer T on top of the visco-elastic half-space has the greatest impact. Higher values of $(a - b)$ as well as high and low initial bulk host rock state variable values θhr decrease the fan width significantly.

The static frictional strength of the faults of 0.6 is high when we consider that crustal faults have fluids.
We agree with the reviewer on this point. However, we assume a typical pore fluid pressure ratio of $\lambda \sim 0.67$ that increases the background pressure to a lithostatic pressure of $PBlith = 60.6MPa$ (line 221). Alternatively, the pore fluid pressure could be included to calculate an effective friction coefficient of 0.6 * (1 - 0.67) = 0.2 at shallower depths This difference in perspectives reflects procedures in different communities. The geodynamics community usually defines an effective friction coefficient by multiplying the fluid pressure ratio with friction, whereas the seismicity community leaves the friction coefficient untouched and works with effective stress or pressure (stress minus fluid pressure). In addition, due to the low initial state on the predefined fault the effective friction coefficient on this fault drops to values around $\mu \sim 0.4$ as the fault is ruptured.

The 20 km choice for maximum fault zone width for the heuristic fault zone thickness, needs stronger substantiation.

We add to line 180:

The upper fault width limit Wmax is defined as the width of inelastic interseismic deformation obtained from fault-parallel GPS and InSAR data. We get a first order estimate of this quantity by measuring the half width of the fault-parallel velocity approaching the far-field plate velocity asymptotically. Wmax can vary significantly between ~ 2 km (Jolivet et al., 2013) and ~ 100 km (Jolivet et al., 2015; Lindsey and Fialko, 2016) in natural faults and depends on the crustal material and thickness, the rate of deformation and the size of the respective fault zone. Consequently, we set Wmax = 20 km as an averaged proxy for the fault width in the interseismic phase. The relation 12 can be interpreted as a heuristic fix to the problem of grid-size-dependent localization in continuum models with RSF.

E. Something to consider in the discussion of the paper is the role of nearby faults on the 'bending' of fault traces. While fault strike may bend in response to changing slip conditions, most crustal faults develop within a complex system where they might interact with nearby faults. Slip on a nearby fault (such as the Garlock fault near the San Andreas) may in many cases have larger impact on the bending of faults than difference in aseismic and coseismic lateral propagation.

This is very right and we agree with the reviewer on these points. Indeed, they were addressed in our manuscript already. Especially in section 3.4, in which we introduce model HPT, we noticed and mentioned fault bending and interaction (line 462):

In the following we analyze several indications of fault and rupture interactions due to stress changes that are typically ignored in seismic cycle models. They include: (1) Rupture arrest when two sub-parallel ruptures get too close to one another. This can be observed for fault HPT001, which stops growing because the stresses on the extensional side of the subsequently forming branch HPT01 increase, get dominant and limit the compressional side stresses of HPT001. As a consequence, only extensional stresses remain at the tip of HPT001, such that the fault gets thinner on its compressional side (Fig. [9c,b]). This leads to (2) a stop in fault growth and fault abandoning. ***Further, fault bending (3) is observed as fault HPT02 approaches HPT0001 and the former starts to bend due to local interactions of stresses. After bending, both faults intersect (4), which causes HPT02 to terminate*** *(5). All together, this behavior is well visible in the video of the HPT simulation, 19 Mb. Consequently, new interjacent branches can stop if their extensional side stress field interacts with the compressional side stress field of another rupture. This is the case when the branches of two subparallel ruptures get close to one another. In this process, the fault on the extensional side is likely to continue extending. This line of reasoning applies for a dextral fault system and is reasonable since the evolving fault structure as a total has an extensional character, which*

means that an extensional stress state is predominant and the extensional fault's side is favored.

We have summarized our findings and have discussed them in section 4.5 (line 608):
The single main fault rupture in this model excites 10 dynamic secondary ruptures on the extensional side bulk that can arrest, bend, converge, intersect and get abandoned. This complexity is linked to variations of the normal stress during and between earthquake sequences, which affect the evolving fault pattern. That behavior highlights the importance to include a varying normal stress in earthquake cycle models instead of assuming a constant normal stress. …
An interesting feature in model HPT is the main fault replacement (or jump). This is reflected in the singular growth and slip activity of the outermost fault branch HPT0001 at the end of the simulation. In the dynamically altered stress field this outermost fault branch is most favorably oriented. A main fault jump was reported in southern California where the San Gabriel fault was originally the main strand of the San Andreas fault, but was replaced at about 4 Ma (Moore and Byerlee, 1991). Faults that are unfavorably oriented for large amounts of slip will be replaced by progressively better oriented faults (Moore and Byerlee, 1989). Fault branch interaction occurs also on the long-term when the stress fields of approaching fault strands start to interfere (manifest in a seismically initiated incipient connection between RT1 and RT2 at x~140 km in Fig. 3). Seemingly, the fault system intends to increase its efficiency by decreasing the fault complexity on the long-term due to fault interaction which can lead to abandoning of abundant fault strands. This is another indication, apart from the previously discussed one, that the fault optimizes its growth efficiency and aims at reaching a steady state on the long-term in which seismic and aseismic growth preferentially happen in the same direction.

Additionally, immature faults may develop bends in their earliest stages when neighboring segments that are not colinear link up to form a single fault surface (Hatem et al., JSG 2017).
We have reported this behavior in the submitted version of the manuscript, already (line 362):
Additionally, faults RT1 and RT2 interact with each other. Fault RT2 starts to bend towards RT1 at 360 years. This behavior is not recorded in the other reference models. Visible is also a seismically initiated connection between RT1 and RT2 at x=130 km that starts at 355 years.

F. The manuscript strives to address a wide range of conditions/questions. I wonder if some parts of the manuscript, such as the HPT models, might be best served as supplemental material.
We would not want to exclude or shift a part that answered the remarks of reviewer 1 posed under previous point **E**.

Specific comments

The paper is very well written. I have a few specific comments that may strengthen the writing in places.

Throughout the manuscript (eg. Line 102, 298 and many others): 'Fault extension' reads a bit odd since extension is a strain term. The text might be clearer with use of 'fault propagation'.
We changed that everywhere.

Line 40 (and there abouts): The use of Riedel terminology for splay fractures strikes me as a bit odd because we typically refer to Riedels as the early formed echelon fault segments. The fractures within the damage zone are more commonly called splay cracks. You may find papers by Cooke (JGR 1997) and Willemse and Pollard (1998) helpful because they show the range of orientation of splay fractures that can develop with different conditions on the fault.
We agree. We changed the respective paragraph and added the reference to Cooke (1997).

Line 51: Define SCEC.
We defined it in the new version of the manuscript.

Line 213: Mixing strain (extensional) and stress (compressional) term. Make these both either strain or stress.
We did not find the term "stress" between lines 211-216. What is the reviewer referring to?

Line 252: spelling of strengthening
We changed that.

Line 253: 'This results' is ambiguous. This what? Being more clear will help the reader. Line 254: Better than what?
We changed that to (line 496):
This contrast of large L and low b in the bulk rock results in intermittent seismic and aseismic growth sequences. We think this behaviour reflects the natural growth of crustal faults better than constant values of L and b, which lead to rapid fault propagation after singular earthquakes. This difference has major implications on the dynamics and geometry of fault evolution, as discussed in the next section.

Line 399 and throughout: I'm not a fan of the acronym OOF for optimally oriented fault model. Why not just spell it out since you already have a lot of acronyms and only use OOF for one section of the paper?
The term OOF is now spelled out in the new version of the manuscript.

Line 497: This is just one paper, for which there is a rich literature. Add e.g. and some more citations.
We added (line 525):
Stress analysis of a crack loaded in mode II explains the formation of tensile fractures at the crack tip (e.g. King and Sammis, 1992; Cooke, 1997; Poliakov et al., 2002; Rice et al., 2005).

Line 540: Another interesting study is a quasi-static dynamic model of Savage and Cooke (JSG 2010). That study differs from the ones citated in that it does not limit damage development along pre-existing mesh. So, the results of Savage and Cooke (JSG 2010) might be interesting to compare to your new model results.
We added (line 572):
The value of the slip-weakening distance was shown to regulate between more continuous along-strike damage and concentrated fracturing at fault tips (Savage and Cooke, 2010).

Line 573-574: This is an interesting result. I believe that this finding confirms results of Jiang and Lapusta – it could be helpful to cite their work here.
Jiang and Lapusta (2016, 2017) use a depth dependent effective normal stress. However, our models feature, on top of a spatially varying effective normal stress (in our case effective pressure), a temporal variation of the effective normal stress (effective pressure). To make it more clear we add to line 609:
This complexity is linked to spatial and temporal variations of the normal stress during and between earthquake sequences, which affect the evolving fault pattern. That behavior highlights the importance to include both spatially and temporally varying normal stress in earthquake cycle models instead of assuming a constant normal stress or only assuming a depth dependent normal stress.

Line 583: There is a rich literature on the development of new faults that are more efficient. Add e.g to this reference.
Thanks, we added that.

Line 594: Cooke (JGR 1997) show that changes in friction distribution near fault tips alters the stress concentration and the angle of the splay crack. The change in friction arises in the transition between mature fault with static friction to immature fault with higher friction. Could this process be contributing to your observation of changing splay angle?
A change in the splay angle occurs due to earthquakes (as discussed in section 4.2) and consequently due to differences between aseismic and seismic fault growth (as discussed in section 4.3). Both depend on the optimality of the pre-existing fault angle (as discussed in section 4.4) and are influenced by fault branch interactions (as discussed in section 4.5). As shown in Preuss et al. (2019) the local friction coefficient at the tip of an aseismically and a

seismically growing fault differ substantially, which leads to different fault orientations. So yes, the transition between a mature fault with a given friction to an immature fault with a different (possibly higher) friction is contributing to the observation of changing splay angles. This finding is extensively mentioned throughout the manuscript and in Preuss et al. (2019). Hence, we do believe a further explanation or interpretation is not needed in section 4.6.

Line 602: Add Cooke (JGR 1997) to this reference list as it is very much related to these other good papers.
Thanks, we added that.

Line 628: The width of the plastic fan in the models is larger than that seen in Savage and Brodsky (2011).
We agree and refer to our answer of the reviewers remark **D** in which we discuss that the size of the plastic off-fault fan is a result of a misorientation of the predefined fault in the reference models. As shown in Figure 8, an optimal oriented fault results in a severe decrease of the plastic fan. To make this clearer we add to line 669:
The width of the plastic fan in our models is larger than that seen in observations from Savage and Brodsky (2011). This difference stems from the non-optimally oriented fault of the reference model, which was discussed under 4.4 and which is compared to an optimally oriented fault with significantly lower off fault yielding in figure 8. Additionally, in our model the width of the fan is controlled by several parameters, of which the thickness of the elastic layer T on top of the visco-elastic half-space has the greatest impact. Too high values of $(a - b)$ and too high and too low initial bulk host rock state variable values θhr decrease the fan width significantly.

Reviewer 2 - Boris Kaus

1.1) Yield stress criteria

You correctly write that at yield F=0, and you employ a standard Drucker-Prager yield function (eq. 9). Yet, your expression for the yield function (eq. 8) is incorrect, which can be best illustrated graphically:

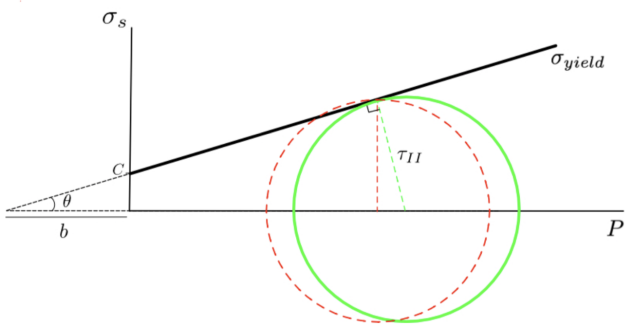

The plot shows the yield function (black) together with the Mohr-Circle (green circle, which has radius II). At yielding (F=0), the Mohr-Circle exactly touches the yield stress function. This condition is not II = yield (your eq. 4), as this gives the red circle (which predicts a stress that is somewhat larger than the yield stress). Instead, we can use trigonometry to compute the condition for F=0. If we define the effective angle of friction as:
tan = I(1 −),
we can define the yield condition (F=0) as: II = sin( ) + cos( )

Since this is correctly described in the textbook of one of the co-authors of this manuscript, I suspect that it is incorporated correctly in the software. I also don't know how big an effect it will make on the results, even if this would not be the case (to be tested). Yet, in any case, it would be good if you can correct your description.

We thank the reviewer for this important comment and a clarifying discussion, which together helped improving the paper.
We clarified the yielding function description and changed notations to avoid confusion. We use a modified Drucker-Prager yielding condition with constant compressive strength and variable friction coefficient.
We changed the method description in line 141:
The onset of plastic deformation is defined by the yield criterion:

F = τII − σc − μeff(RSF) Peff,

where Peff = P − Pfluid = P (1 − λ) with the pore fluid pressure factor λ = P /Pfluid , σc is the constant compressive strength that marks the residual strength at P = 0 and μeff(RSF) is a variable effective friction parameter that we define based on our continuum

RSF formulation. We use a modified Drucker−Prager plastic yield function (Drucker and Prager, 1952) in the form:

$\sigma_{yield} = C(RSF) + \mu(RSF)\, P_{eff}$,

where

$\mu(RSF) = \tan(\sin^{-1}(\mu_{eff}(RSF)))$ is the local friction coefficient that is widely used and obtained form laboratory experiments

and

$C(RSF) = \sigma_c/\cos(\sin^{-1}(\mu_{eff}(RSF)))$ is the local cohesion.

The local effective friction parameter $\mu_{eff}(RSF)$ evolves according to the invariant reformulation of rate- and state-dependent friction for a continuum, introduced by Herrendörfer et al. (2018). This formalism was applied to freely and spontaneously growing seismic and aseismic faults by Preuss et al. (2019), by interpreting how plastic deformation starts to localize and forms a shear band that approximates a fault zone of finite width that can host earthquakes. Localized bulk deformation and fault slip are related by defining the plastic slip rate Vp as

$V_p = 2\varepsilon'_{II}(p)W$,

where W denotes the width of the fault zone in the continuous host rock. We formulate $\mu_{eff}(RSF)$ as:

$\mu_{eff}(RSF) = a \operatorname{arcsinh}(V_p/2V_0 \exp((\mu_0 + C/P + b \ln(\theta V_0/L))/a))$,

where a and b are laboratory-based, empirical RSF parameters that quantify a direct effect and an evolution effect of friction, respectively, L is the RSF characteristic slip distance, μ_0 is a reference friction coefficient at a reference slip velocity V_0 (Lapusta and Barbot, 2012), and C is the cohesion as part of the state variable θ (Marone et al., 1992) that evolves according to the aging law:

$d\theta/dt = 1 - V_p\theta/L$.

Additionally, we updated Figure 4 according to the recomputed relative fault angles based on equation 9.

1.2) Elastic material parameters

Your choice of having the same values for bulk and shear moduli (table 1; both 50 GPa) results in a Poisson ratio of 0.125. That might be appropriate for already damaged rocks, but perhaps not so much for intact rocks. How sensitive are your results to the particular choice of Poisson ratio?

We thank the reviewer for this question. A Poisson's ratio of 0.125 is on the lower end of values for rocks, but still common for a wide range of rocks as for example shown in *Poisson's ratio values for rocks* (H. Gercek, 2007). Furthermore, we tested a range of shear moduli resulting in varying Poisson's ratios and found only a marginal impact on the model results. In particular, the main messages of our manuscript are not influenced by changes in the Poisson's ratio. We illustrate this by comparing the snapshots of simulations with Poisson's ratio of 0.125 and 0.25. We focus on the dynamically generated off-fault yielding at approximately the same deformation stage just before the rupture hits the end of the predefined fault. Both snapshots are attached. The differences comprise:

- First earthquake nucleates 75 years later for ν = 0.25.
- The maximum slip velocity is ~ 0.08 m/s higher for ν = 0.25.
- The off-fault splay localization is more irregular with a higher degree of localization and a slightly higher off-fault reach for ν = 0.25.

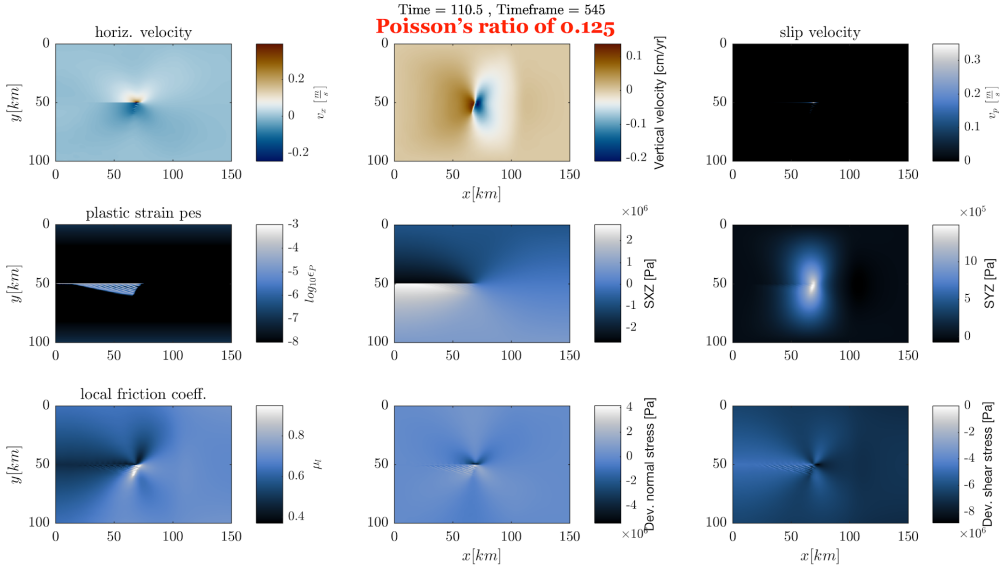

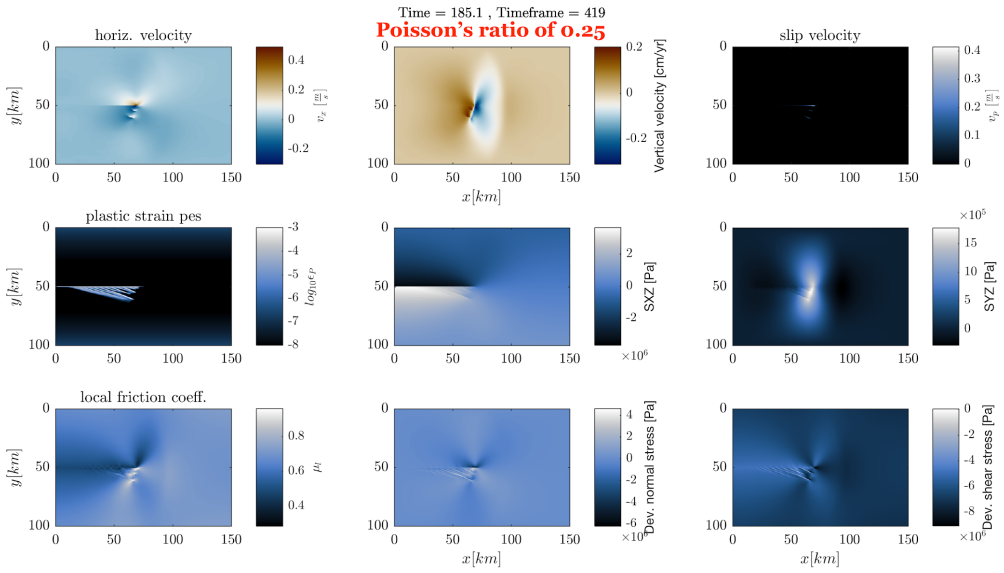

In light of our answer above we add to line 703 of the manuscript:
Our choice of parameters results in a Poisson ratio of 0.125. Such a relatively low Poisson's ratio is on the lower end of values for rocks, but still common for a wide range of rock types as for example shown in Gercek (2007). To illustrate the impact of different Poisson's ratios we have tested a range of different shear moduli resulting in varying Poisson's ratios. These tests have shown that the main messages of our manuscript are not influenced by changes in the Poisson's ratio.

2) Minor remarks:

- Table 1: I suppose that the host rock cohesion is 6 MPa, and not 6e6 MPa?
  This is correct. We changed that.

- Fig. 3: you show an overview of several different models. Yet, are the snapshots chosen to have approximately the same plastic strain, deformation stage or time? Would be good to mention it.
  Thanks for this comment. We added the following to the figure caption:
  The snapshots in [a] are chosen to have approximately the same deformation stage with regard to fault length 'R*1'. Model RW constitutes an exception as RW1 remains
  very short (1.8 km, see main text).

- Figure 4. It would be good to explain at the beginning of the figure caption that this figure concerns the RT model.
  We agree and added a short note.

- Your movies are extremely large (some over 1 Gb!); it is certainly possible to create smaller movie-sizes from a set of pictures, and I believe that this is important for readers that do not have a high bandwidth connection.
  We agree. All movies are now approx. 5 times smaller with a maximum size of 122 Mb. These smaller videos can be uploaded upon resubmission.

Characteristics of earthquake ruptures and dynamic off-fault deformation on propagating faults

Simon Preuss[1], Jean Paul Ampuero[2], Taras Gerya[1], and Ylona van Dinther[3]

[1]Geophysical Fluid Dynamics, Institute of Geophysics, Department of Earth sciences, ETH Zürich, 8092 Zürich, Switzerland
[2]Géoazur Laboratory, Institut de Recherche pour le Développement - Université Côte d'Azur, Campus Azur du CNRS, 06560 Valbonne, France
[3]Tectonics, Department of Earth Sciences, Utrecht University, Princetonlaan 4, 3584 CB, Utrecht, the Netherlands

Correspondence: Simon Preuss (sipreuss@ethz.ch)

Abstract. Natural fault networks are geometrically complex systems that evolve through time. The evolution of faults and their off-fault damage pattern are influenced by both dynamic earthquake ruptures and aseismic deformation in the interseismic period. To better understand each of their contributions to faulting we simulate both earthquake rupture dynamics and long-term deformation in a visco-elasto-plastic crust subjected to rate-and-state-dependent friction. The continuum mechanics-based numerical model presented here includes three new features. First, a 2.5-D approximation to incorporate effects of a viscoelastic lower crustal substrate below a finite depth. Second, we introduce a dynamically adaptive (slip-velocity-dependent) measure of fault width to ensure grid size convergence of fault angles for evolving faults. Third, fault localization is facilitated by plastic strain weakening of bulk rate-and-state friction parameters as inspired by laboratory experiments. This allows us to for the first time simulate sequences of episodic fault growth due to earthquakes and aseismic creep. Localized fault growth is simulated for four bulk rheologies ranging from persistent velocity-weakening to velocity-strengthening. Interestingly, in each of these bulk rheologies, faults predominantly localize and grow due to aseismic deformation. Yet, cyclic fault growth at more realistic growth rates is obtained for a bulk rheology that transitions from velocity-strengthening friction to velocity-weakening friction. Fault growth occurs under Riedel and conjugate angles and transitions towards wing cracks. Off-fault deformation, both distributed and localized, is typically formed during dynamic earthquake ruptures. Simulated off-fault deformation structures range from fan-shaped distributed deformation to localized ~~Riedel~~ splay faults. We observe that the fault-normal width of the outer damage zone saturates with increasing fault length due to the finite depth of the seismogenic zone. We also observe that dynamically and statically evolving stress fields from neighboring fault strands affect primary and secondary fault growth and thus that normal stress variations affect earthquake sequences. Finally, we find that the amount of off-fault deformation distinctly depends on the degree of optimality of a fault with respect to the prevailing but dynamically changing stress field. Typically, we simulate off-fault deformation on faults parallel to the loading direction. This produces a 6.5-fold higher off-fault energy dissipation than on an optimally oriented fault, which in turn has a 1.5-fold larger stress drop. The misalignment of the fault with respect to the static stress field thus facilitates off-fault deformation. These results imply that fault geometries bend, individual fault strands interact and that optimal orientations and off-fault deformation vary through space and time. With our work we establish the basis for simulations and analyses of complex evolving fault networks subject to both long-term and short-term dynamics.

1 Introduction

Immature strike-slip faults accumulate displacement over time as they undergo a slip localization process. On the long-term, these structures can become deeply penetrating, major faults that represent a highly localized weak zone through the lithosphere (Norris and Toy, 2014). The majority of slip is thereby confined to the cores of the principal faults (Chester et al., 1993). Most prominent examples, like the San Andreas and the North Anatolian fault systems, span lengths of several hundreds of km (e.g., Sibson, 1983). ~~Strike-slip faults generally grow laterally~~ Analogue experiments have shown that strike-slip faults can initiate by upward propagation and linkage of an early set of echelon faults to form a through-going fault (e.g. Tchalenko, 1970; Hatem et al., 2017). Further growth towards a through-going strike-slip fault generally occurs due to lateral propagation and the structural fault complexity usually increases towards the younger portions at the fault tip (Perrin et al., 2016a; Cappa et al., 2014). In this area diverse fault patterns and fault networks are found. Analog experiments, structural geology and fracture mechanics define a variety of different secondary fault structure types: branching faults, one-sided horsetail splay faults, synthetic and antithetic Riedel ~~splays,~~ faults, splay cracks, wing cracks and mixed modes ~~(e.g. Hubert-Ferrari et al., 2003; Kim et al., 2004; Mitchell and Faulkner, 2009; Aydin and Berryman, 2010; Perrin et al., 2016b, Fig. 1 b,c~~ (e.g. Cooke, 1997; Hubert-Ferrari et al., 2003; Kim et al., 2004; Mitchell and Faulkner, 2009; Aydin and Berryman, 2010; Perrin et al., 20 . The different types mainly differ in fault angle and fracture mode. For example, R Riedel ~~splays~~ shears that form in response to Coulomb failure make an angle of $10° - 20°$ with the main fault (Riedel, 1929; Logan. et al., 1979; Logan et al., 1992), while opening-mode wing cracks grow in the direction of the most tensile circumferential stress and hence have a greater angle (Erdogan and Sih, 1963; Ashby and Sammis, 1990). The terms 'shear fracture', 'splay' and 'splay fault' are used as equivalents in this study. R1 refers to synthetic Riedel shears and R2 refers to antithetic conjugate Riedel shears often also named R'.

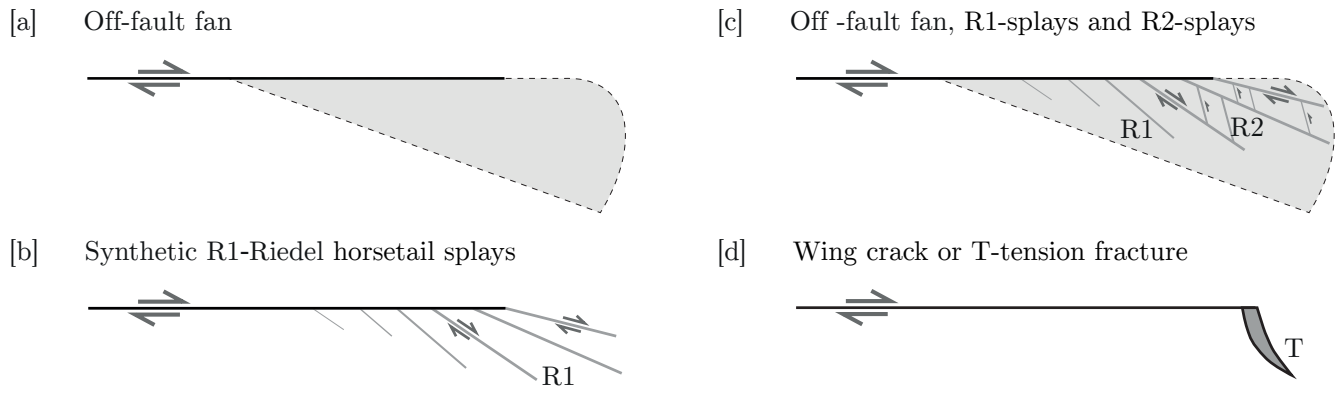

Figure 1. Fault structures developing at the tip of a sliding strike-slip fault. Modified from (Kim et al., 2004) and combined with schematic interpretations from (Faulkner et al., 2011) and (Perrin et al., 2016b). R1 = synthetic Riedel shear fracture, R2 = antithetic conjugate Riedel shear fracture and T = tension fracture or wing crack.

The secondary fault structures altogether constitute the wake of a permanent off-fault damage zone (Scholz et al., 1993; Manighetti et al., 2004; Perrin et al., 2016b), alternatively termed off-fault fan (Fig. [1 a,c]). This fan is also present around

very well localized principal slip zones (Shipton et al., 2006). Field observations indicate that the damage fan width scales with accumulated fault displacement (Perrin et al., 2016b, a). At a smaller distance from each fault, an inner damage zone of micro-fractures also develops, whose width does saturate at a few 100 m for larger displacements (Mitchell and Faulkner, 2009; Savage and Brodsky, 2011; Ampuero and Mao, 2017). During an earthquake, energy is dissipated in the damage zone over large distances from the fault (Cappa et al., 2014; Ampuero and Mao, 2017). Earthquakes do not only operate on the main fault structure but can also propagate on secondary faults (Mitchell and Faulkner, 2009). The damage zone also contributes to long term deformation. For example, secondary faults in California accommodate up to 43% of the total fault slip rate of mapped faults taken from the ~~SCEC catalog~~ Southern California Earthquake Center Community Fault Model (data from Plesch et al., 2017).

Initial attempts to simulate plastic off-fault deformation in elastodynamic earthquake mechanics models were undertaken by Andrews (1976). The plastic fan width was directly related to the rupture propagation distance (Andrews, 2005; Rice et al., 2005). Factors controlling the extent and distribution of off-fault plasticity during dynamic rupture were analyzed by Templeton and Rice (2008). The effect of plasticity on transitions between different rupture styles was studied and the prestress angle was shown to have an influence on rupture speed, plastic zone width and rotation angle of the total seismic moment (Gabriel et al., 2013). A theoretical and numerical study of 3-D rupture with off-fault plasticity revealed how the seismogenic depth of a fault limits the width of the inner damage zone (Ampuero and Mao, 2017). Dynamic earthquake ruptures were shown to propagate along self-chosen paths of a simplified, persistent, branched fault geometry (e.g. Bhat et al., 2004, 2007). Formation of localization in dynamically generated damage zones was linked to branched faults in a micromechanics based model allowing for the incorporation of crack growth dynamics (Bhat et al., 2012). A recent 2-D dynamic earthquake rupture modeling study nicely shows coseismic off-fault damage during earthquake ruptures at different depths and analyzes its contribution to the overall energy budget (Okubo et al., 2019). Geometrically more complex faults and elastic-plastic off-fault response due to singular events in non-evolving media were studied in a generic case (Fang and Dunham, 2013) or in a realistic fault geometry model of the Landers earthquake (Wollherr et al., 2019). The main limitation of all these modeling studies is that they are restricted to one single earthquake, a fixed and mostly single main fault that is unable to extend, simplified background stress state represented by a fixed orientation of the principal stress (e.g. Okubo et al., 2019), and an artificial nucleation for numerical convenience (e.g. Gabriel et al., 2013; Okubo et al., 2019). A first attempt to study dynamic branching in self-chosen crack paths was undertaken by Kame and Yamashita (2003). Their study shows crack bifurcation into two branches in homogeneous elastic media. Their modelling approach does not account for visco-elasto-plastic media and recurrent coseismic events interspersed by aseismic interseismic phases. Recent efforts have advanced the timescales of the simulations to model earthquake cycles on strike-slip faults governed by rate-and-state friction in 2-D antiplane (vertical cross-section) with off-fault plasticity (Erickson et al., 2017). However, 2-D antiplane approaches can not model horizontal propagation of strike-slip faults and their off-fault branches, and models with diffuse plastic deformation can not simulate localized off-fault branches explicitly. Nor can these dynamic models grow fault branches interseismically.

In this manuscript we develop a computational model that combines the following features: dynamic off-fault yielding in a visco-elasto-plastic material, long-term evolution of a geometrically complicated fault system, consistent simulation of

multiple subsequent earthquakes on the same fault system, effect of the finite seismogenic-elastic depth. Our method builds upon and extends the recently developed STM-RSF numerical model for Seismo-Thermo-Mechanical modeling under Rate-and-State Friction (van Dinther et al., 2013b; Herrendörfer et al., 2018; Preuss et al., 2019) to, for the first time, simulate cyclic seismic and aseismic fault growth. The STM model was developed in van Dinther et al. (2013b, a) to bridge long geodynamic time scales of fault and lithosphere evolution with short time scales approximating earthquake sequences in a visco-elasto-plastic medium. It was extended to simulate spontaneous off-fault events in van Dinther et al. (2014). Herrendörfer et al. (2018) developed the STM-RSF version to simulate sequences of earthquakes with time steps down to milliseconds using a new invariant rate-and-state friction (RSF) formulation on predefined, mature faults. Preuss et al. (2019) extended the STM-RSF code to simulate aseismic and seismic fault growth. However, once a fault was formed and ruptured dynamically in a velocity-weakening bulk medium it continued to rupture indefinitely if unhindered by model boundaries.

To accurately simulate cyclic fault growth with off-fault plasticity we extend this STM-RSF framework with three new features. First, we compare four different rate-dependent rheologies in the bulk material. The most realistic one is inspired by laboratory friction experiments and includes a weakening of RSF parameters with plastic strain (e.g. Beeler et al., 1996; Marone and Kilgore, 1993). These rheologies allow us to simulate distributed and localized coseismic off-fault deformation during dynamic rupture propagation, spanning all the possibilities presented in figure 1. Second, we expand the 2-D framework to 2.5-D using a generalized Elsasser approach (Lehner et al., 1981). Recent work has shown that the thickness of the plate has a direct effect on the width of the inner damage zone leading to a saturation as a function of rupture length (Ampuero and Mao, 2017). The 2.5-D approximation accounts for stresses generated at depth to counteract sudden displacements originated from a crustal earthquake. It allows us to analyze which factors control the width of the damage zone. Third, we introduce a new rate-dependent fault width formulation to avoid mesh dependency of our simulation results, an issue raised in previous numerical work (e.g. Templeton and Rice, 2008; Bhat et al., 2012). Ultimately, with this new set of models we study the spatio-temporal evolution of an (a)seismically extending pre-existing main fault. Application of driving plate velocities at the boundaries of the crustal block result in the concentration of stresses on the fault, which leads to consecutive earthquakes. These sudden dynamic events are interspersed by aseismic periods (interseismic phases). The two processes together shape the long-term structure of the fault system by extending the main fault. The mode of ~~extension~~ propagation depends on various properties of the host rock. We compare the orientations of the newly developed faults to the predictions of classical Mohr-Coulomb failure theory and distinguish aseismic from seismic growth contributions. Furthermore, we test the role of the optimality of the angle of the pre-existing fault on the amount of coseismic off-fault deformation. Various implications of our results are discussed in section 4.

2 Methods

We summarize the main ingredients of the STM-RSF modeling approach in section 2.1, but refer the reader to Herrendörfer et al. (2018) for more details. This description focuses on incorporating three new model ingredients: a 2.5-D approximation

(section 2.1), a dynamically adapting fault width during the localization process (section 2.2), and a plastic strain dependent bulk rheology ~~behavior~~ behaviour as described in the model setup (section 2.3).

2.1 Seismo-mechanical modeling with rate- and state-dependent friction and a 2.5-D approximation

We expand the 2-D STM-RSF framework to 2.5-D using a generalized Elsasser approach introduced by Rice (1980); Lehner et al. (1981). The 2.5-D model captures the concept that rapid deformation in the elastic-brittle upper crust exerts a shear stress load onto the deeper visco-elastic crustal substrate, which then relaxes slowly and transfers stresses back to the upper crust (Lehner et al., 1981). Assuming, for simplicity, a Maxwell coupling between the upper and lower crust, the shear tractions at their interface are approximated as thickness-averaged stresses (ch. 10 in Rice, 1980). Weng and Ampuero (2019) showed that the energy release rate of dynamic ruptures in a 2.5-D model approximates very well that of long ruptures with finite seismogenic depth in a 3-D model. The 2.5-D simulations thus approximately account for the 3-D effect of a finite rupture depth at the same computational cost as a 2-D simulation.

In 2.5-D we solve for the conservation of mass:

$$\rho \frac{\partial v_i}{\partial x_i} = -\frac{D\rho}{Dt}, \tag{1}$$

and the conservation of momentum:

$$\frac{\partial \tau_{ij}}{\partial x_j} - \frac{\partial P}{\partial x_i} = \rho \frac{Dv_i}{Dt} - \rho g_i, \tag{2}$$

where $i = 1, 2$ and $j = 1, 2, 3$ are coordinate indices, x_i and x_j represent spatial coordinates, ρ denotes density, $\frac{D}{Dt}$ is the material time derivative, v_i is velocity and g_i is gravity. P is the dynamic total pressure, defined as positive under compression, and computed from the mean stress as:

$$P = -\frac{\sigma_{kk}}{3}, \qquad \text{with } k = 1, 2, 3, \tag{3}$$

The deviatoric stress tensor τ_{ij}, with $i = j = 1, 2$, in the crust is given as:

$$\tau_{ij} = \sigma_{ij} + \delta_{ij} P, \tag{4}$$

with σ_{ij} being the Cauchy stress tensor and δ_{ij} the Kronecker delta. They are linked to deviatoric strain rates $\dot{\varepsilon}'_{ij}$ by the following visco-elasto-plastic constitutive relationship (Gerya and Yuen, 2007):

$$\dot{\varepsilon}'_{ij} = \frac{1}{2G} \frac{\overset{\nabla}{D}\tau_{ij}}{Dt} + \frac{1}{2\eta} \tau_{ij} + \dot{\varepsilon}'_{II(\text{plastic})} \frac{\tau_{ij}}{\tau_{II}}, \tag{5}$$

where G is the shear modulus, $\frac{\overset{\nabla}{D}}{Dt}$ denotes the co-rotational time derivative, η is the effective ductile viscosity in the crust, $\dot{\varepsilon}'_{II(\text{plastic})}$ is the second invariant of the deviatoric plastic strain rate and $\tau_{II} = \sqrt{{\tau_{11}}^2 + {\tau_{12}}^2 + {\tau_{13}}^2 + {\tau_{23}}^2}$ is the second invariant of the deviatoric stress tensor in 2.5-D. The stresses at depth are averaged over the thickness of the crust T as (Lehner et al., 1981):

$$\tau_{i3} = \frac{G_S \, u_i}{bT} + \frac{\eta_S \, \dot{u}_i}{T_S}, \tag{6}$$

where u_i are the displacements averaged over the thickness of the crust, T, and T_S is the thickness of the lower crustal substrate with shear modulus G_S and viscosity η_S, respectively. The geometric factor $b = 1/\pi^2$ is designed to match the energy release rate between 2.5-D and 3-D dynamic rupture simulations (Weng and Ampuero, 2019). The medium is compressible, so density and pressure are related by

$$\frac{D\rho}{Dt} = \frac{\rho}{K}\frac{DP}{Dt}, \tag{7}$$

where K is the bulk modulus. The onset of plastic deformation is defined by the yield criterion ~~$F = 0$ with a~~ :

$$F = \tau_{II} - \sigma_c - \mu_{\text{eff}}(\text{RSF})\, P_{\text{eff}}, \tag{8}$$

where $P_{\text{eff}} = P - P_{\text{fluid}} = P(1-\lambda)$ with the pore fluid pressure factor $\lambda = P/P_{\text{fluid}}$, σ_c is the constant compressive strength that marks the residual strength at $P = 0$ and $\mu_{\text{eff}}(\text{RSF})$ is a variable effective friction parameter that we define based on our continuum RSF formulation. We use a modified Drucker-Prager plastic yield function (Drucker and Prager, 1952) in the form:

$$F = \tau_{II} - \sigma_{yield} = C(\text{RSF}) + \mu(\text{RSF})\, P_{\text{eff}}, \tag{9}$$

~~with local pressure-dependent yield strength~~ where

$\sigma_{yield}\mu(\text{RSF}) = \tan(\sin^{-1}(\mu_{\text{leff}}(1-\lambda\text{RSF})P + C,))$ is the local friction coefficient that is widely used and obtained from laboratory exp

(10)

~~where μ_l is the local friction coefficient (it can vary both in space and time), C denotes cohesion (residual shear strength at zero effective pressure P), and λ is the pore fluid pressure factor (ratio between fluid pressure and solid pressure). The local friction coefficient~~ and

$C(\text{RSF}) = \sigma_c/\cos(\sin^{-1}(\mu_{\text{eff}}(\text{RSF})))$ is the local cohesion. (11)

The local effective friction parameter $\mu_{\text{eff}}(\text{RSF})$ evolves according to the invariant reformulation of rate- and state-dependent friction for a continuum, introduced by Herrendörfer et al. (2018). This formalism was applied to freely and spontaneously growing seismic and aseismic faults by Preuss et al. (2019), by interpreting how plastic deformation starts to localize and forms a shear band that approximates a fault zone of finite width that can host earthquakes. Localized bulk deformation and fault slip are related by defining the plastic slip rate V_p as

$$V_p = 2\dot{\varepsilon}'_{II(p)} W, \tag{12}$$

where W denotes the width of the fault zone in the continuous host rock. We ~~write equation 9 as:~~ formulate $\mu_{\text{eff}}(\text{RSF})$ as:

$$\sigma_{yield} = \mu_{\text{leff}}(1-\lambda\text{RSF})P = a\,\text{arcsinh}\left[\frac{V_p}{2V_0}\exp\left(\frac{\mu_0 + \frac{C}{P} + b\ln\frac{\theta V_0}{L}}{a}\right)\right] P(1-\lambda), \tag{13}$$

where a and b are laboratory-based, empirical RSF parameters that quantify a direct effect and an evolution effect of friction, respectively, L is the RSF characteristic slip distance, μ_0 is a reference friction coefficient at a reference slip velocity V_0 (Lapusta and Barbot, 2012), and C is the cohesion as part of the state variable θ (Marone et al., 1992) that evolves according to the aging law:

$$\frac{d\theta}{dt} = 1 - \frac{V_\mathrm{p}\theta}{L}. \tag{14}$$

To solve the governing equations we use an implicit, conservative finite-differences scheme on a fully staggered grid combined with the marker-in-cell technique (Gerya and Yuen, 2003, 2007). All details of the numerical technique that comprise the STM-RSF code can be found in Herrendörfer et al. (2018).

2.2 Slip-velocity-dependent fault-width formulation

In contrast to previous studies, in which fault width W in the slip-rate formulation of friction was constant (e.g., van Dinther et al., 2013b, a; Herrendörfer et al., 2018; Preuss et al., 2019), we introduce here a dynamically adapting W. Deformation localizes to within 1-2 grid cells in classical applications of plasticity (e.g., Lavier et al., 2000; Buiter et al., 2006; van Dinther et al., 2013a). In models involving a pre-existing fault, Herrendörfer et al. (2018) found that setting $W = \Delta x$ leads to convergence with respect to grid size. However, this choice is not optimal in models involving the spontaneous formation of a fault, because it leads to grid-size-dependent fault orientations (on the order of a few degrees) and earthquake onset times (Preuss et al., 2019). This results from the elastic loading phase, in which, for larger grid sizes, the same slip velocity is scaled to a smaller effective plastic strain rate. This yields a higher visco-plastic viscosity and thus, higher stresses, resulting in a larger slip velocity. This higher slip velocity, in turn, leads to a faster evolution of state and thus, to a faster localization of deformation. The higher stresses additionally induce a higher local friction coefficient in the undeformed matrix and hence, the fault angle becomes larger (Preuss et al., 2019). To prevent this dependence on grid size, we introduce a length scale in the relationship between slip rate and plastic strain rate that incorporates the distributed deformation during the fault localization phase, which may span more than one grid cell.

We propose a new invariant continuum-based RSF formulation, in which the fault width W adapts dynamically as a function of the slip velocity V_p during the strain localization phase. We define a rate-dependent width

$$W_{V_\mathrm{p}} = W_\mathrm{max}\ \log\left(1 + K\frac{V_0}{V_p}\right) \tag{15}$$

and complement it with lower and upper bounds as

$$W = \begin{cases} W_\mathrm{max}, & \text{if } W_{V_\mathrm{p}} \geq W_\mathrm{max} \\ W_{V_\mathrm{p}}, & \text{if } W_\mathrm{max} \geq W_{V_\mathrm{p}} \geq \Delta x \\ \Delta x, & \text{if } W_{V_\mathrm{p}} \leq \Delta x \end{cases} \tag{16}$$

The dimensionless scaling parameter $K = 1$ determines the onset of localization. ~~We set the~~ The upper fault width limit ~~$W_\mathrm{max} = 20$ km based on averaged values from~~ W_max is defined as the width of inelastic interseismic deformation obtained

from fault-parallel GPS and InSAR data~~across several natural faults . The above relation~~ . We get a first order estimate of this quantity by measuring the half width of the fault-parallel velocity approaching the far-field plate velocity asymptotically. $W_{\max}$ can vary significantly between ~ 2 km (Jolivet et al., 2013) and ~ 100 km (Jolivet et al., 2015; Lindsey and Fialko, 2016) in natural faults and depends on the crustal material and thickness, the rate of deformation and the size of the respective fault zone. Consequently, we set $W_{\max} = 20$ km as an averaged proxy for the fault width in the interseismic phase. The relation 15 can be interpreted as a heuristic fix to the problem of grid-size-dependent localization in continuum models with RSF. We base this fix on the fact that slow crustal movements in the interseismic period lead to distributed deformation (Collettini et al., 2014), e.g., within the Pacific-North America plate boundary, which is very wide in the north, across the San Andreas fault and the Eastern California shear zone segments (Wdowinski et al., 2007). On the other hand, faults show localization of deformation during coseismic periods, sometimes identifiable at large depths by the presence of pseudotachylyte (Sibson, 1977, 1983; Swanson, 1992; Norris and Toy, 2014; Ikari, 2015). Examples of highly localized slip planes are numerous, in different rock types and on different scales (e.g., Chester et al., 1993; Chester and Chester, 1998; Sibson, 2003; Smith et al., 2011; Barth et al., 2013; Collettini et al., 2014; Rice, 2017). Also laboratory experiments reveal that strain is initially distributed across the full thickness of a sheared gouge layer, but after some displacement it localizes to a high-strain principal slip surface (Smith et al., 2015; Ritter et al., 2018a, b). These principal slip surfaces, which seem to be a prerequisite for future earthquake slip, form at subseismic slip velocities (Ikari, 2015). This ~~behavior~~ behaviour is affirmed by numerous experimental and microstructural studies that report a fine-grained shear localization zone cut by a discrete principal slip zone during sliding at seismic velocities (e.g., Toro et al., 2004; Brantut et al., 2008; Han et al., 2010; Scuderi et al., 2013; Paola et al., 2015; Pozzi et al., 2018). Alloy in extension and compression shows an analogous sequence of formation of coarse deformation bands followed by shear strain localization leading to crack formation (Price and Kelly, 1964). A common mode of failure in granular materials involves the same pattern of localization of homogeneous deformation into a narrow zone of intense shear (Jenkins, 1990). In addition, our heuristic fix follows the general tendency for logarithmic rate-dependency of materials, which appears in, e.g., friction and porosity/dilatancy (Dieterich, 1981; Logan and Rauenzahn, 1987; Sleep, 1995; Segall and Rice, 1995; Beeler et al., 1996; Chen et al., 2017).

The result of using the new slip-velocity-dependent fault-width formulation is that both the fault angle and the onset times of earthquakes converge with grid size (appendix A).

2.3 Model setup

Our 2.5-D model setup represents a generic case to study the evolution of a fault zone within a plane-strain crust of 20 km thickness coupled to an underlying lower crustal layer of 20 km thickness. The model horizontal size is 250 km x 150 km. The third dimension is reduced by depth-averaging, leading to a 2.5-D model (section 2.1). The initial fault is prescribed as a 120 km long line of lower state θ and zero cohesion C compared to the host rock. It represents the tip of a mature fault in nature and will be the locus of stress concentration leading to the spontaneous nucleation and propagation of a rupture as a mode II crack. The experimental geometry, together with the Dirichlet v_x-velocity boundary conditions applied in opposite directions at the back and front boundaries, represent a dextral strike slip zone (Fig. [2]).

Table 1. Rate- and state-dependent friction (RSF) and material parameters of the four 2.5-D reference models

Parameters	Symbol	Value
Upper Crust		
Thickness	T	20 km
Shear modulus	G	50 GPa
Bulk modulus	K	50 GPa
Density	ρ	2700 kg/m^3
Shear wave speed	c_s	4.3 km/s
Effective viscosity	η	$5{\cdot}10^{26}$ Pa s
Initial mean stress (pressure)	P_B	20 MPa
Gravity	g_i	0 m/s^2
Reference effective-static friction coefficient	μ_0	0.6
Cohesion		
Host rock	C_{hr}	6 ~~$\cdot 10^6$~~ MPa
Fault	C_{f}	0 MPa
Initial state		
Host rock	θ_{hr}	$\frac{L}{V_0}\exp(30)$ s $\approx 8.5 \times 10^8$ years
Fault	θ_{f}	$\frac{L}{V_0}\exp(-1)$ s ≈ 0.03 years
Reference slip velocity	V_0	$4{\cdot}10^{-9}$ m/s = 12.6 cm/yr
Reference model rate-strengthening *RS*		
Characteristic slip distance		
Host rock	L_{hr}	1.0 m
Fault	L_{f}	0.01 m
RSF direct effect	a	0.011
RSF evolution effect		
Host rock	b_{hr}	0.007
Fault	b_{f}	0.017
Reference model rate-neutral *RN*		
Characteristic slip distance		
Host rock	L_{hr}	0.01 m
Fault	L_{f}	0.01 m
RSF direct effect	a	0.011
RSF evolution effect		
Host rock	b_{hr}	0.011
Fault	b_{f}	0.011
Reference model rate-weakening *RW*		
Characteristic slip distance		
Host rock	L_{hr}	0.01 m
Fault	L_{f}	0.01 m
RSF direct effect	a	0.011
RSF evolution effect		
Host rock	b_{hr}	0.017
Fault	b_{f}	0.017
Reference model rate-transitioning *RT*		
Characteristic slip distance		
Host rock	L_{hr}	1.0 $\rightarrow$ 0.01 m (if ε_p 0 $\rightarrow$ 5e-4)
Fault	L_{f}	0.01 m
RSF direct effect	a	0.011
RSF evolution effect		
Host rock	b_{hr}	0.007 $\rightarrow$ 0.017 (if ε_p 0 $\rightarrow$ 5e-4)
Fault	b_{f}	0.017
Lower crustal substrate		
Thickness	T_{S}	20 km
Shear modulus	G_{S}	50 GPa
Viscosity	η_{S}	$1{\cdot}10^{17}$ Pa s

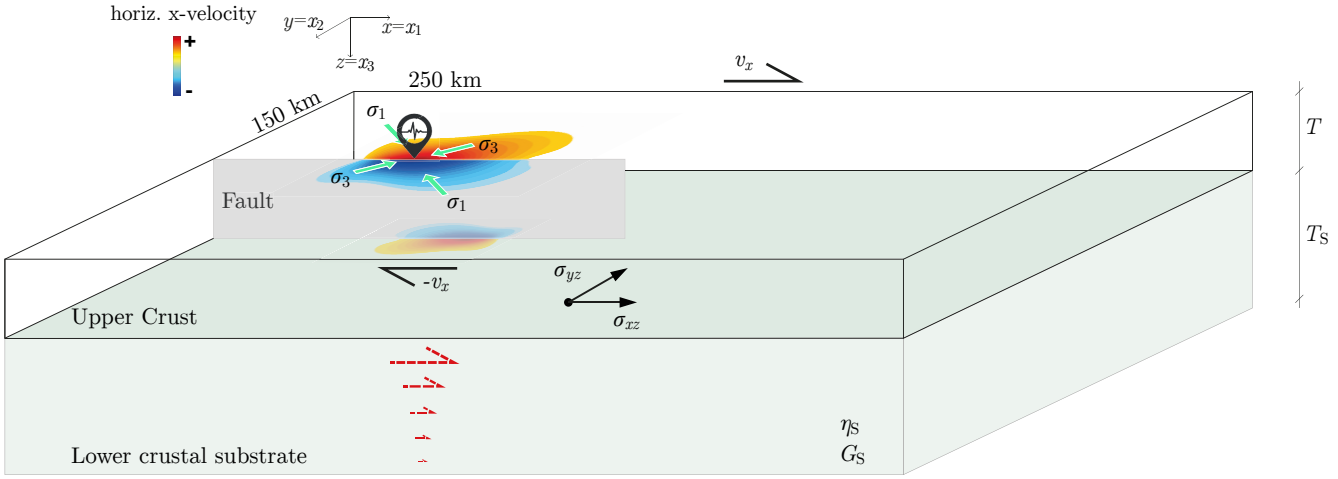

Figure 2. 2.5-D model setup of the dextral inplane strike slip simulation: 2-D box of size 250 km x 150 km with 501 x 301 nodes in x- and y-direction, respectively (grid resolution of 500 m). Each cell contains 16 markers, resulting in 2,400,000 global mobile markers. Bold black shear-arrows indicate direction of Dirichlet v_x-velocity boundary conditions applied in opposite direction: $v_x = \pm 2 \cdot 10^{-9}$ m/s $= \pm 6.4$ cm/yr. At left and right boundaries, Neumann boundary conditions for v_x are prescribed. Velocity v_y is set to zero at all boundaries. The 120 km long fault (in gray) has a lower state θ compared to the host rock. The third (z) dimension is approximated by a depth-averaging of upper crustal stresses due to a relaxed lower crustal substrate (section 2.1). A symbolic earthquake rupture occurring on the fault is shown by horizontal x-velocity contours in red-blue at the location of a seismic wave sign. Light green arrows with white contour mark the direction of the principal compressional stresses, the maximum one, σ_1, is initially oriented at $45°$. The counteracting effect of the rupture on stresses in the relaxed substrate is shown by the red dashed arrows. The directionality of shear tractions σ_{xz} and σ_{yz} on the lower surface of the upper crust is represented by black arrows with triangle heads. Quantities η_S, G_S and dimensions T and T_S are listed in table 1.

The maximum compressive stress σ_1 is initially oriented at an angle of $45°$ to the imposed shear direction, indicated by the light green arrows in Fig. [2] (e.g., Meyer et al., 2017). Values of the reference model parameters (Table 1) are set largely in accordance with Lapusta et al. (2000), with differences in the choice of V_0 and the initial mean stress P_B. Following Herrendörfer et al. (2018), we set V_0 equal to the loading rate. The background effective pressure $P_B = 20$ MPa can be related to the lithostatic pressure $P_{B_{\text{lith}}}$ and the pore fluid pressure P_f by

$$P_B = P_{B_{\text{lith}}} - P_f = P_{B_{\text{lith}}}(1 - \lambda). \tag{17}$$

Considering a typical value of pore fluid pressure ratio $\lambda \sim 0.67$, the lithostatic pressure is $P_{B_{\text{lith}}} = 60.6$ MPa, which is equivalent to a depth of 2.3 km, representing the upper crust. In section 3.2.1 we simulate at higher and lower pressures that represent higher and lower depths, respectively.

In this study we present four different reference models with varying RSF ~~behavior~~ behaviour in the bulk: model *RS* has rate-strengthening ~~behavior~~behaviour, model *RN* has rate-neutral ~~behavior~~behaviour, model *RW* has rate-weakening ~~behavior~~behaviour, and model *RT* has a transition from rate-strengthening to rate-weakening ~~behavior~~ behaviour at increasing plastic strain. We

choose to study these different bulk ~~behaviors~~ behaviours because in the literature of materials and geology both strain-rate-strengthening and strain-rate-weakening are reported to be possible and sufficient conditions for localization of deformation (Hobbs et al., 1990). By studying these different bulk ~~behaviors~~ behaviours we are able to emphasize their different characteristics. In the first three cases, $(a-b)$ and L are kept constant in the entire model domain, respectively. In model RT, $(a-b)$ and L decrease with plastic strain (Table 1), motivated by laboratory observations (Beeler et al., 1996; Scuderi et al., 2017; Marone and Kilgore, 1993).

3 Results and analysis

In the first part of this section we present and compare the results of the four models to understand the effects of a rate-sensitive bulk rheology on off-fault deformation and fault growth. We then focus on two reference models to further investigate factors influencing the off-fault fan width and the role of visco-elastic lower crust relaxation on short-term and long-term off-fault deformation (section 3.2). In section 3.3 we study the role of the angle of the predefined fault on off-fault deformation. Finally, we analyze the formation of localized secondary branches (section 3.4).

3.1 Role of rate-dependent bulk rheology on off-fault deformation and fault growth

The initial elastic loading phase takes 325.5 years in all four reference models. In this initial stage stresses start to localize on the predefined fault and its slip velocity increases exponentially (Fig. [3b]). About 5.5 years after the slip velocity reaches the plate velocity, an earthquake nucleates on the fault at x=0 km and propagates eastwards along the fault. During the earthquake, the on-fault slip rate V_p rises to seismic slip velocities, as defined by the typical dynamic scale V_{seis} introduced by Rubin and Ampuero (2005) (Fig. [3b]). The generation of coseismic off-fault plastic deformation is a general feature of our models (Fig. [3a]). It occurs on the extensional side of the fault, which is ~~favored~~ favoured over the compressional side when the maximum principal compressional stress direction is $\geq 45°$ (Kame et al., 2003). The off-fault plastic zone grows continuously in a fan-like manner but eventually its thickness (fault-normal size) saturates at a value of $\sim$8 km and at a rupture distance of $\sim$80 km. Concurrently, the slip velocity reaches a maximum at $V_p = 1.1$ m/s. The maximum width of the off-fault fan H_{max} and the onset of saturation are affected by various parameters investigated in section 3.2.1.

Besides these general similarities among the four reference models we note two main differences. First, the plastic zones off the main fault have distinct characteristics. A fan of diffuse deformation occurs in models RS and RT, while localized deformation on secondary faults occurs in models RN and RW. Thus, the type of plastic off-fault yielding depends on the properties of the bulk rheology. Only a rate-neutral or rate-weakening material in which L is comparatively low (0.01 m) allows for fault localization in the off-fault material. Each of the secondary fault branches is formed by individual secondary dynamic ruptures during the first main fault rupture. This localization ~~behavior~~ behaviour will be addressed further in section 3.4.

The second main difference is that only model RT hosts a sequence of several earthquakes. In the other three models the entire new fault geometry forms during a single earthquake, an aftershock and the subsequent post-seismic and inter-seismic

phases. Before more seismic events can nucleate, the main fault has already extended by aseismic growth toward a model boundary and the simulation is stopped to prevent boundary effects. ~~Thus, models~~ The models with constant rate-sensitivity (models RS, RN, and RW~~have in common that fault growth during the earthquakes contributes only a small portion to the total formed fault length F_L (Fig. 3b). Furthermore, their fault growth~~) have fast fault growth rates of up to 77 km/yr that are much faster than in model ~~RT. We follow that a bulk rheology with constant rate-sensitivity favors a faster fault growth. In contrast, the heterogeneities introduced by a weakening of the RSF parameters L and b slow down the faulting process due to the absorption of energy by the weakening mechanism. As a consequence, the faults in model RT can extend in alternating seismic and aseismic growth periods. Only if the region ahead of the fault tip has experienced distinct plastic strain and L and b are altered to create a rate-weakening fault earthquakes can propagate on there. Otherwise, dynamic rupturing is hindered in the intact bulk, where L is still high and b is still low and rate-strenghtening, respectively. This results in intermittent seismic and aseismic growth sequences. We think this behaviour reflects the natural growth of crustal faults better. This difference has major implications on the dynamics and geometry of fault evolution, as discussed in the next section. Nevertheless,~~ RT. Despite this major difference, all reference models have in common that fault growth during the earthquakes contributes only a small portion to the total formed fault length F_L (Fig. [3b]).

In the following analysis we mainly focus on models RW and RT because the off-fault characteristics of models RW and RN are similar, as well as those of models RT and RS. Furthermore, RW and RT represent the two cases of dominant higher-angle and lower-angle continuing faults, respectively. In that way, RW and RT are the most diverse end member cases of the four reference models. At the same time model RT is the most realistic model with successive earthquakes, distributed deformation and localized fault growth. Model RW on the other hand allows for strong off-fault localization and tends towards irregular fault patterns with unevenly spaced secondary fault branches.

3.1.1 Temporal and geometrical evolution of fault growth

As the main fault propagates beyond the tip of the predefined fault, all four reference models form two new faults with two orientations. A “higher-angle fault” forms with a high angle compared to the strike of the predefined fault. It is an antithetic conjugate Riedel shear fault and is termed ’R*2’, where ’*’ stands for the different reference models. A “lower-angle fault” forms with a lower strike angle and is a synthetic Riedel shear fracture termed ’R*1’ hereafter. Detailed analysis of model RT reveals that these two faults are formed because the main fault rupture induces two stress lobes on the extensional side of the fault. These zones were studied by Poliakov et al. (2002) who termed them ’secondary faulting area’. These areas also evoke lobe-like anomalies of the dynamic friction value. Later on, the frontal lobe is responsible for the formation of RT1 and the back lobe forms the conjugate fault RT2 (Fig. [4a,b]). This ~~behavior~~ behaviour of model RT is representative for all four reference models. We confirm that both faults form according to the Mohr-Coulomb failure criterion at either the Coulomb-fault angle (R1 fault) or the conjugate angle (R2 fault). These angles α are

$$\alpha = \pm\left(\frac{\pi}{4} \mp \frac{\varphi}{2}\right), \tag{18}$$

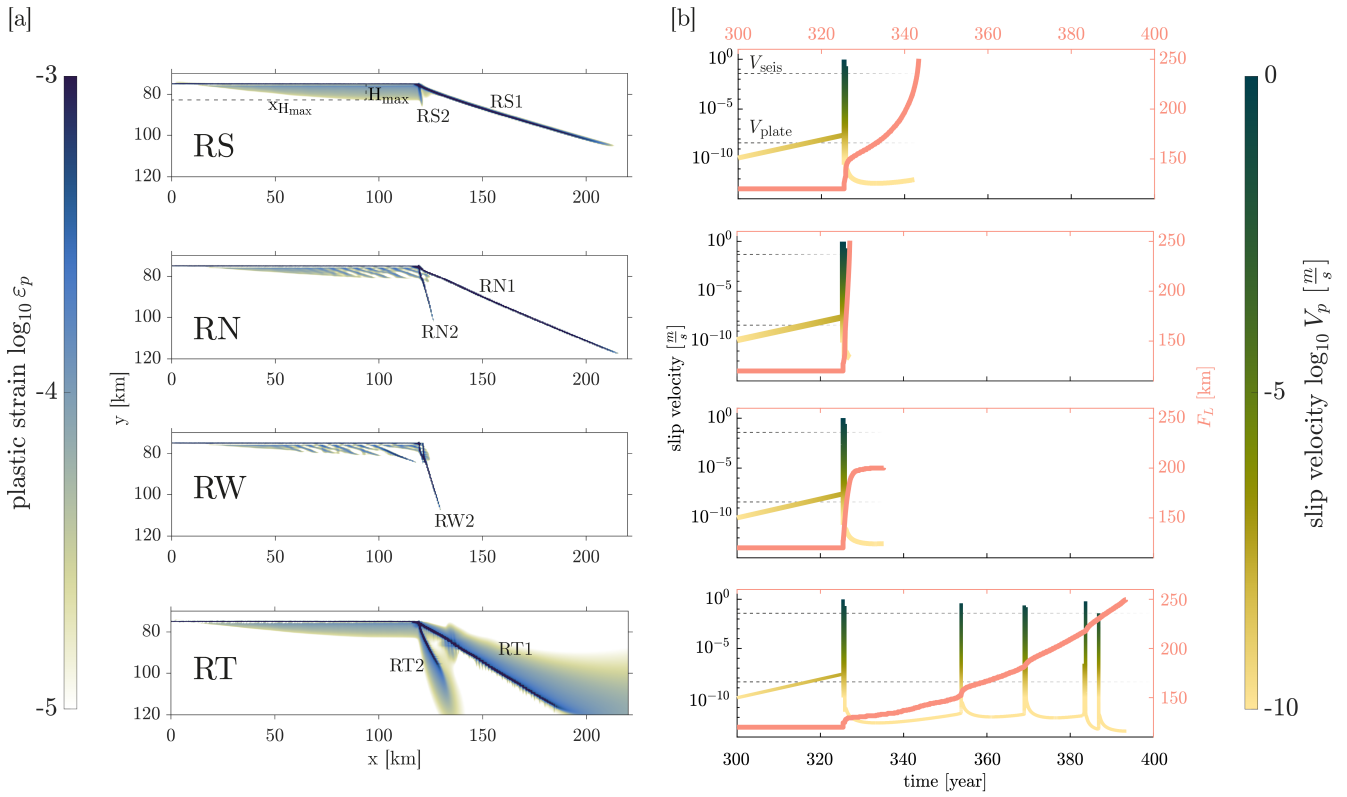

Figure 3. Summary of four different right-lateral reference models. [a]: Simulation results in form of plastic strain pattern: RS= rate-strengthening, RN= rate-neutral, RW = rate-weakening, RT = transition from RS to RW. 'R*1' indicates a Riedel fault (lower strike angle), 'R*2' refers to the conjugate Riedel fault (R') with a higher strike angle compared to the R1-Riedel shear, respectively. The snapshots in [a] are chosen to have approximately the same deformation stage with regard to fault length 'R*1'. Model RW constitutes an exception as RW1 remains very short (1.8 km, see main text). [b]: Temporal evolution of the plastic slip velocity V_p inside the fault at (x, y) = (100 km, 75 km) until end of simulation. The seismic threshold velocity is indicated as V_{seis}. Red line shows the fault length F_L over time.

where φ denotes the internal angle of friction, related to ~~μ_l,~~ the local friction coefficient μ(RSF) that we call μ_l for simplicity in the following, by $\mu_l = \tan\varphi$. The angle α spans between the maximum principal compressional stress direction σ_1 and β, the angle of the newly forming fault, such that $\alpha = \sigma_1 - \beta$ (Fig. 4c). The reference angle is the horizontal shear direction. The compressive state of stress in our simulation limits α: $\alpha_1 = 45° - (\varphi/4)$ and $\alpha_2 = -45° + (\varphi/4)$ (conjugate). We take the average of σ_1 and μ_l to compute the resulting α at 3 different instants: 1) five seconds before fault ~~extension~~propagation, 2) one minute after the initiation of the first fault ~~extension~~propagation, and 3) 25 years after the initial fault ~~extension~~ propagation (Fig. [4d], symbols ■, ●, ♦, respectively). These data reveal that the local dynamic conditions in the proximity of faults determine the angles of the faults RT1 and RT2, which was previously reported for an isolated growing fault (Preuss et al., 2019). Additionally, they approach the theoretical angle α and converge on it with advancing time (Fig. [4d]). This ~~behavior~~ behaviour indicates that the absolute fault angles β of RT1 and RT2 are predictable, even before the faults have formed. As

soon as the two lobes are formed by elevated stresses near the rupture front, i.e. approximately 10 seconds after the earthquake nucleation, they have the potential to determine the angle of the R-fault and the R2-conjugate (Fig. [4e]). Both RT1 and RT2 exhibit a lower final strike angle than their predictions during the dynamic phase. This is justified by the fact that seismically growing faults have a higher strike angle than aseismically forming faults (Preuss et al., 2019). Thus, the seismically initiated fault decreases in strike angle as soon as the slip velocity transitions to the non-seismic range. This happens as the rupture hits the undeformed host rock. Indeed, at the end of the first earthquake the fault extends in a pure seismic mode and the angle of the new fault is greater than in the following interseismic phase after the earthquake. Hence, both RT1 and RT2 flatten in the 0.3 years right after the first earthquake and before the aftershock. This ~~behavior~~ behaviour is visible in the online videos (link to video ~~,,,~~RT, 116 Mb, RS, 41 Mb, RN, 41 Mb, RW, 68 Mb) just after the first earthquake, in Fig. 4b and in all four reference model snapshots (Fig. [3a]).

The different reference models ~~favor~~ favour either of the two fault angle types or develop them jointly. The smaller the initial L and $a-b$ in the bulk material, i.e. with more weakening, the higher the tendency to ~~favor~~ favour the high-angle conjugate fault (Fig. 3). This ~~behavior~~ behaviour is evident if one compares models RS and RW. An intermediate situation occurs in models RN and RT when both fault types are well developed and evolve in an approximately equal manner. A second result of lower initial L and $a-b$ is the greater generated fault length in response to the primary seismic event: $F_L = 12.3$ km (RW2), 11.3 km (RN2), 8.3 km (RS2) and 7.4 km (RT2). Hence, an earthquake can extend a fault farther in a rate-weakening material than in a rate-strengthening material, and the rate-transition case produces the shortest seismic growth. The aseismic fault growth rate in a rate-neutral material is higher than in a rate-strengthening material (Fig. [3b]). Most likely it is even higher in a rate-weakening material but a comparison is impeded because model RW ~~favors~~ favours a different fault growth path.

In the following we describe the evolution of the R1-fault and the conjugate R2 in detail for the four individual model cases (link to video ~~,,,~~RT, 116 Mb, RS, 41 Mb, RN, 41 Mb, RW, 68 Mb). In the RS model with pure rate-strengthening ~~behavior~~ behaviour RS1 and RS2 are created simultaneously as the seismic rupture penetrates into the bulk, and they are equally long. Then, the left-lateral RS2 transitions into a passive state, gets abandoned and stops growing, while the right-lateral branch RS1 extends aseismically. We record no pronounced off-fault deformation for either RS1 nor RS2. They are rather localized fault strands that are wider than the newly formed faults in the other models, however.

In the rate-neutral model the propagating rupture excites several equidistant secondary splay faults that form under the same Coulomb-angle (R1) and saturate at x$\sim$80 km, such that they are 16.5 km long as a maximum. As the main rupture and the secondary ruptures penetrate into the bulk, two of the secondary splay faults that were triggered by the dynamic main fault rupture continue to grow by $\sim$5 km at a constant Coulomb-angle, and then get abandoned. Simultaneously, the main rupture initiates RN1 and RN2 under the respective Coulomb-angles of the Riedel shear and the conjugate shear. Right after the earthquake, the left-lateral RN2 is $\sim$4 times longer than RN1. However, right-lateral RN1 is increasingly ~~favored~~ favoured as both fault branches extend in an aseismic manner and RN1 finally becomes the main extension of the predefined fault. The aseismic phase in which RN1 extends by 130 km and grows towards the right boundary lasts for 1.2 years.

In the rate-weakening model RW the secondary splay faults form earlier than in model RN, and are more localized and partly non-equidistant. Particularly apparent is a secondary splay at x$\sim$105 km that is highly localized and causes a stress shadow

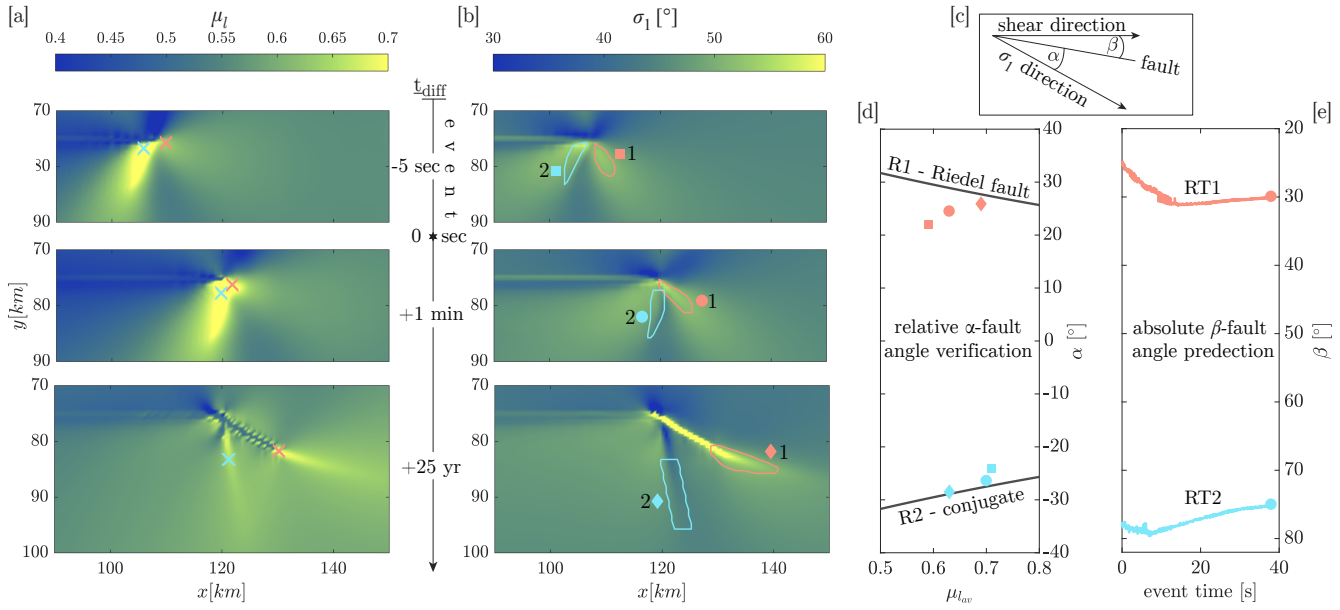

Figure 4. Evolution of local friction coefficient and stress orientation of model RT over time and prediction of the absolute fault angle. 3 different times are: 1) Five seconds before fault ~~extension~~ propagation (symbol ■), 2) One minute after the initiation of the first fault ~~extension~~ propagation (symbol ●), and 3) 25 years after the initial fault ~~extension~~ propagation (symbol ♦). Red color represents the Coulomb angle of R1 and turquoise refers to the conjugate fault R2. [a]: Snapshot zooms of the local friction distribution μ_l at different times. Crosses indicate the location of the two maxima of μ_l at the rupture tip or at the tip of the newly formed fault, respectively. [b]: Snapshot zooms of the distribution of the maximum compressive stress orientation σ_1 at different times. Red and turquoise polygons indicate the locations around the frictional maxima inside the two stress lobes where μ_l and σ_1 are sampled and averaged according to two standard deviations of the mean (95th percentile). [c]: Schematic geometrical relation in physical space between horizontal shear direction, σ_1-direction and forming fault. β represents the absolute fault angle, α is the angle between fault and σ_1-direction, such that $\alpha_{1,2} = \sigma_1 - \beta_{1,2}$. [d]: Relation between averaged local friction coefficient $\mu_{l_{av}}$ and fault angle $\alpha_{1,2}$, which is obtained from the average σ_1-directions for the three different instants shown in [a] and [b] for R1 and R2, respectively. The values from the frontal lobe result in the data converging on the R1-Riedel angle α_1, the data from the back lobe converge on the R2-conjugate α_2. Black lines indicate the theoretical angle given by equation 18. [e]: Prediction of the absolute fault angles $\beta_{1,2}$ for both RT1 and RT2 from sampling averages of μ_l and σ_1 during the entire first dynamic earthquake.

on its compressional side leading to a splay gap. It thus prevents an equidistant spacing of the secondary splays and changes the angles of the subsequent forming splays. We investigate this ~~behavior~~ behaviour in section 3.4. As the secondary splays propagate into the bulk at the fault tip they generate approximately 7 km of new fault surface under the conjugate angle of fault RW2 which they are flanking. Subsequently, the secondary faults and the conjugate RW2 merge. In contrast to models RS and RN, model RW reveals a very weakly localized and short incipient fault RW1 (1.8 km). This fault stops growing because the stresses on the compressional side of the compound of secondary branches and the sinistral conjugate RW2 are dominant and limit the extensional side stresses of short RW1. Thus, RW1 remains short and abandoned after the earthquake until the

simulation stops, such that the sinistral RW2 constitutes the unique extension of the main fault. The simulation RW stops as branch RW2 approaches the lower y-boundary at a higher angle. Consequently, the maximum fault length F_L is shorter than in the other models.

The off fault deformation pattern in the rate-transition model is composed of similar features as model RS. The two branches RT1 and RT2 form as the main fault rupture penetrates into the undeformed bulk. The fault evolution in model RT spans over several earthquake cycles (Fig. 5). Both branches RT1 and RT2 are well developed like in the model RN. However, on the long-term branch RT1 grows faster than RT2 during both aseismic and seismic fault growth stages. It is noticeable that the incipient faults in model RT are surrounded by a wide fan of plastic strain that is absent in the other reference models. This fan arises because both RT1 and RT2 host seismic ruptures in contrast to the newly evolving faults in the other reference models. Thus, a plastic fan like the fans next to the predefined fault can grow. Additionally, more strain is accumulated due to a slower fault growth rate (Fig. 3), which prolongates the model run time compared to the other models and facilitates the formation of distributed strain zones. Strikingly, the fan of fault RT1 is on the compressional side, which is due to the increased angle of RT1 relative to the predefined fault where the fan is on the extensional side. Hence, the angle between RT1 and σ_1 is smaller than $45°$, which implies yielding on the compressional side of the fault. In contrast to the three other reference models, faults RT1 and RT2 exhibit notable changes in the absolute fault angle β. These bends are ascribed to the difference between lower-angle aseismic and higher-angle seismic fault growth, respectively (Preuss et al., 2019). The repeated sequences of seismic growth increase the overall angle of RT1 compared to RS1 and RN1. Nevertheless, the overall growth contribution in model RT is dominated by aseismic growth. This is well visible in figure 5 where the aseismic growth increments are opposed to the seismic ones. Seismic fault growth is mainly limited to the first earthquake where the off-fault damage and the fault ~~extensions~~ branches RT1 and RT2 are created. In the subsequent evolution only marginal portions of fault ~~extension~~ propagation are ascribed to coseismic events. This seismic contribution is accumulated at the outer edges of the interseismically deformed regions (figure 5). The reasons and implications of these findings are discussed in section 4. Additionally, faults RT1 and RT2 interact with each other. Fault RT2 starts to bend towards RT1 at 360 years. This ~~behavior~~ behaviour is not recorded in the other reference models. Visible is also a seismically initiated connection between RT1 and RT2 at x=130 km that starts at 355 years. In summary, the strike angle of the formed faults increases from rate-strengthening to rate-neutral to rate-weakening material. The case of a transition from RS to RW describes a more complex case with intermittent aseismic and seismic growth, fault bends, fault interaction and additional off-fault deformation. In addition, the degree of new fault localization is highest in model RW and follows the order RW-RN-RT-RS.

3.2 Role of a visco-elastic substrate on off-fault deformation

In this section we first analyze the properties of the saturating plastic off-fault fan and study the determining parameters for this saturation. Secondly, we study the long-term effects of the relaxed visco-elastic substrate on the growth of the splay fault fan.

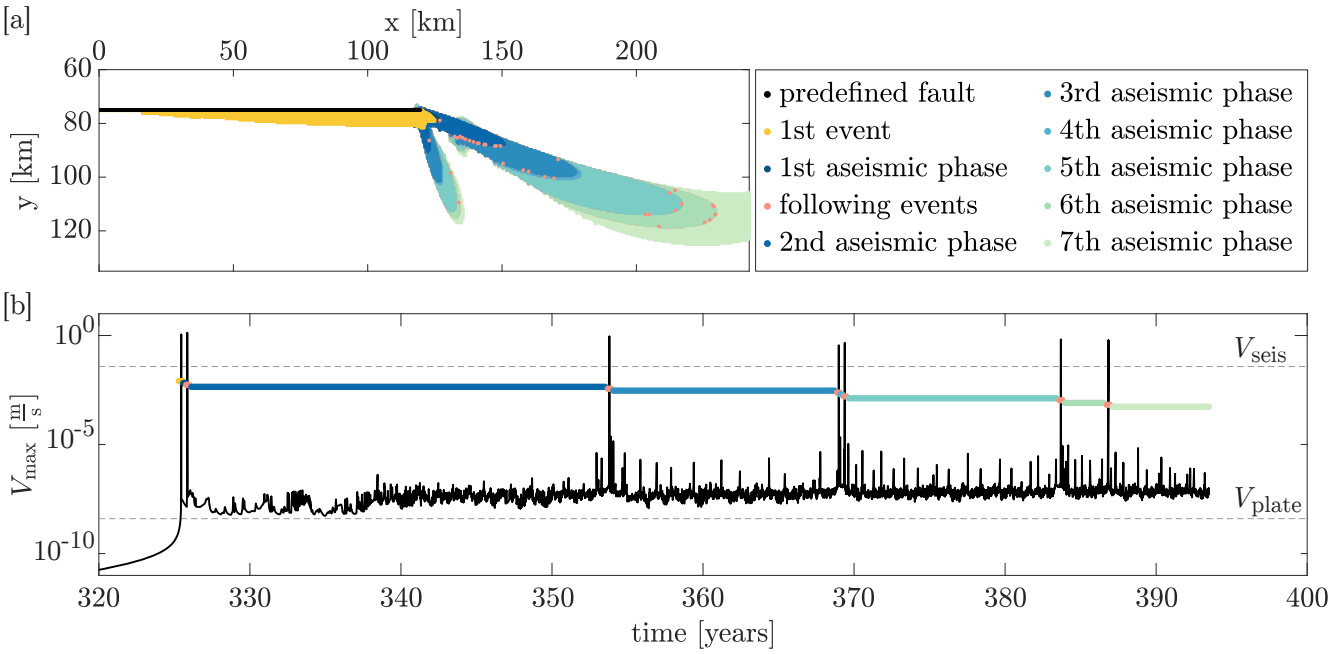

Figure 5. Temporal and spatial evolution of model RT with indication of aseismic and seismic fault growth stages in color. [a]: Accumulated plastic strain exceeding ε_p > 4e-5 for different growth stages. [b]: Logarithm of the global maximum slip velocity $\log(V_{\max})$. A video of the simulation can be found in the online material link to video model RT, 116 Mb

3.2.1 Off-fault fan and saturation

In all four reference models the plastic off-fault fan reaches a maximal width $H_{\max}$ at distances over x∼80 km. The onset distance of the saturation does not depend on the bulk rheology. However, $H_{\max}$ varies from 8.7 km in model RS to 8.2 km in model RT to 6.4 km in model RN to 6.2 km in model RW. In figure 6a we show that the slip during the first earthquake saturates, i.e. the rupture develops a flat slip profile. The reason for this ~~behavior~~ behaviour is the transition from a crack-like to a pulse-like rupture, which can be seen in the steep tapering off of the slip velocity (a healing front) in figure 6b when the rupture front reaches a distance x∼80 km. This transition to a steady pulse-like rupture results from the finite seismogenic depth. In 3-D rupture models, a healing front emerges when the rupture front reaches the bottom of the seismogenic zone, and then travels back to the surface, turning the initial crack-like rupture into a pulse. This interpretation of the saturation of the plastic zone thickness, based on dynamic fracture mechanics and 3-D simulations, was first proposed by Ampuero and Mao (2017). In our 2.5-D approach we do not model the actual rupture front nor the healing front at depth. However, the counteracting response of the visco-elastic substrate in the conservation equation of momentum (Eq. 2) captures the effect of stress transfer from depth to surface. The thickness T_S of the lower crustal substrate can be set arbitrary large and is irrelevant for the model outcome.

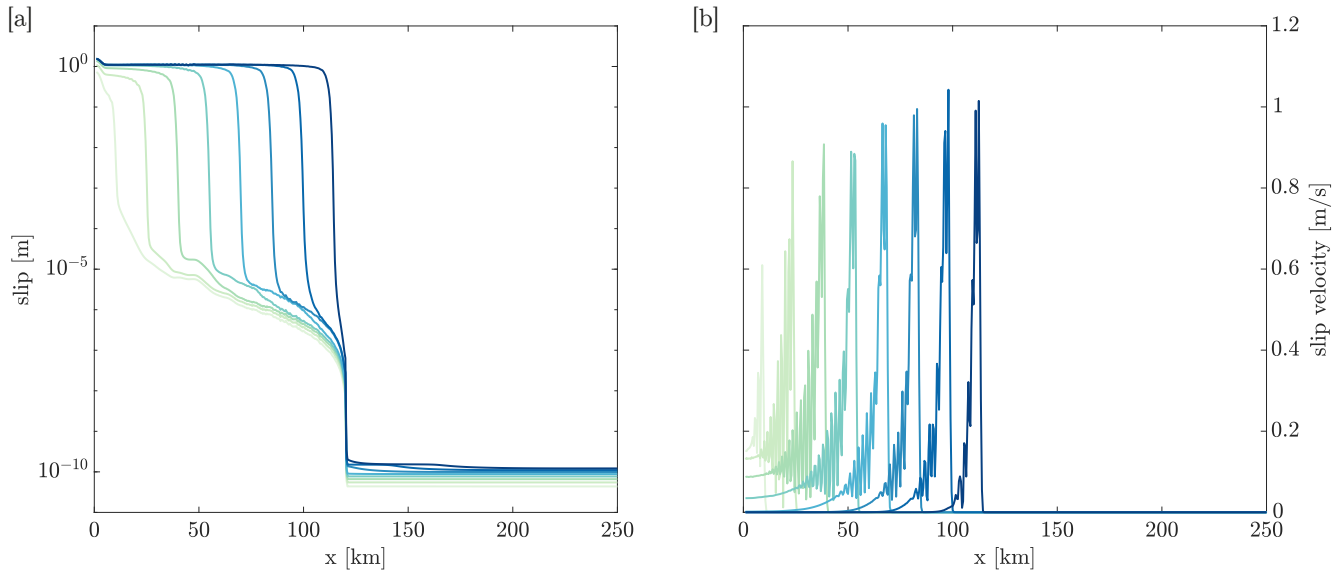

Figure 6. Accumulated plastic slip and slip velocity during the first earthquake on the main fault plotted in 5 s intervals.

We investigate the impact of crustal thickness T, initial background pressure P, initial bulk host rock state variable θ_{hr} and $(a-b)$ on the maximum plastic fan width H_{max} for model RT. In our simulation the fan width increases proportional to the crustal thickness T (Fig. [7a]). The onset distance of the saturation $x_{H_{\text{max}}}$ is also proportional to T (Fig. [7e]). Both characteristics are due to the 2.5-D effect of our simulation. In essence, this T-H_{max}-relation agrees with the simulation data of Ampuero and Mao (2017, inset of figure 13.5 therein). However, our simulation results coincide better with the theoretically determined linear relation between H_{max} and T at large T than with the nonlinear trend in the 3-D simulation (Ampuero and Mao, 2017). This is due to a small ratio (nucleation size)/(seismogenic depth) = 0.5 in our simulations, which ~~favors~~ favours a faster covergence of the curve to the linear trend. Furthermore, the different values of H between both studies are due to different plastic strain cut-off levels used in the definition of H.

We additionally vary the initial background pressure P from 10 MPa to 40 MPa in steps of 10 MPa and find that the maximum fan width converges to H_{max} ~8.5 km, which is 0.3 km wider than H_{max} of the reference model RT (Fig. [7b]). This implies that H_{max} is less sensitive to variations in lithostatic pressure with depth than to the crack-to-pulse-like rupture transition induced by the depth of the seismogenic zone. Our result is consistent with the theory of Ampuero and Mao (2017, their equation 13), who found that the maximum fan width is independent of normal stress. A reduction and increase of the initial host rock state variable θ_{hr} reveals that the value corresponding to the reference model results in the greatest fan width, while higher and lower state values lead to a reduction of H_{max} (Fig. [7c]). A change in $(a-b)$ from 0.001 to 0.01 shows that the fan width H_{max} converges to a value of 6.4 km for decreasing $(a-b)$, which corresponds to the fan width of the rate-neutral model in which bulk $(a-b)$ = 0 (Fig. [7d]). However, since bulk $(a-b)$ is positive in model RT that we analyze here, no localization is reported in contrast to model RN or model RW. A maximum in the $(a-b)$-H_{max}-relation is reached

for $(a-b)$ = 0.006 with $H_{\max}$ = 10 km. If $(a-b)$ is increased above 0.006 the fan width drops to values below 4 km. This is due to a factor 2 decrease of the slip velocity $V_{p_{\max}}$ (Fig. [7f]). Although $V_{p_{\max}}$ seems to be anti-correlated with $H_{\max}$, which in particular is observable for the crustal thickness and pressure model variations, it has an impact on the fan width in the case of higher $(a-b)$.

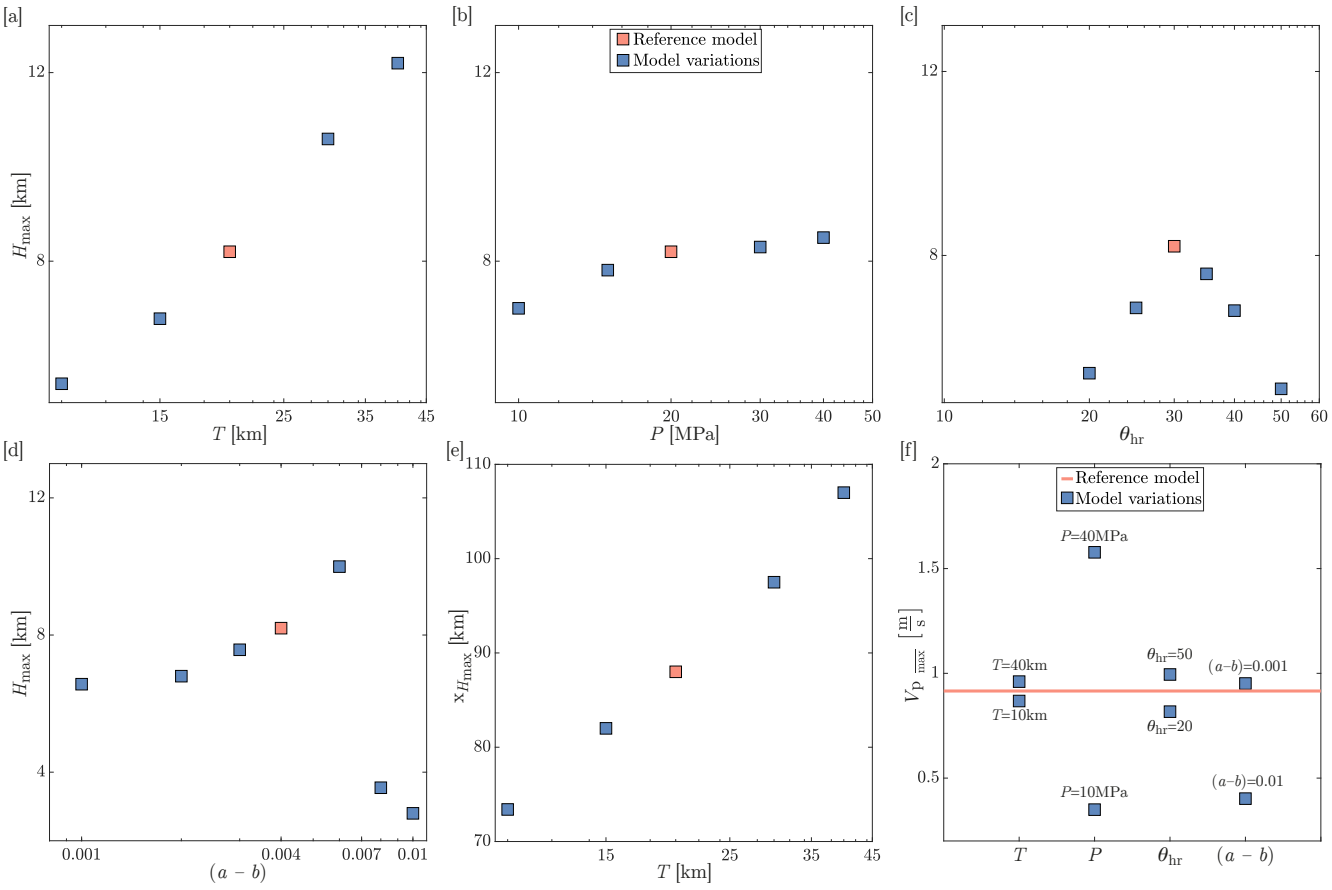

Figure 7. Impact of various parameters on the maximum plastic fan width $H_{\max}$: [a]: Crustal thickness T; [b]: Initial background pressure P; [c]: Initial bulk host rock state variable θ_{hr} and [d]: $(a-b)$. [e]: Relation between onset of the saturation $x_{H_{\max}}$ and T. [f]: Average slip velocity during the first earthquake $V_{p_{\max}}$ as a function of the highest and lowest parameter of each of the four model variations (T, P, θ_{hr}, $(a-b)$), respectively.

3.3 Role of the predefined fault angle on off-fault deformation

In sections 3.1 and 3.2.1 we demonstrated that the plastic strain produced during the first earthquake reaches similar values for all four reference models. In the presence of localized deformation (models RN and RW) the splay faults form at a greater angle than the predefined main fault. Thus, the optimal angle of a newly forming fault in a dynamically elevated stress field

does not coincide with the predefined fault strike. We suppose that the majority of the off-fault strain in these models is due to a 'misalignment' of the predefined fault together with the dynamic reorientation of stresses. In order to prove this supposition we design ~~model OOF~~ a model with an optimally oriented fault in which the predefined fault strike is at 15° to the horizontal shear direction. This is the optimal strike angle, which we obtain by inserting the static friction coefficient $\mu_0 = 0.6$ in equation 18. The parameters of ~~model OOF~~ the model with an optimally oriented fault are based on model RT. In figure 8 we compare the amount of plastic off-fault energy between model RT and ~~OOF~~the model with an optimally oriented fault. While the reference model RT reaches typical plastic energy values and a typical ratio of on-fault to dissipated off-fault plastic energy (e.g., similar to Okubo et al., 2019), these values for ~~model OOF~~ the optimally oriented fault model are substantially lower. In fact, ~~model OOF~~ the latter model exhibits almost no off-fault deformation (Fig. [8a]) and the amount of plastic energy dissipated to the off-fault material is only 0.2 % (Fig. [8c]). This means that the different strike angle of ~~model OOF~~ the optimally oriented fault model reduces the magnitude of the off-fault stresses and thus the reach of off-fault deformation. The minor off-fault deformation starting at x $\approx$ 90 km is due to the dynamic reorientation of stresses, which leaves the pre-existing fault slightly misaligned with the dynamic stress field at high slip velocities.

In figure [8b] we compare the dynamic stress drop between model RT (3.9 MPa) and ~~model OOF~~ the optimally oriented fault model (5.8 MPa). The difference of 1.9 MPa reveals that more energy is concentrated on the predefined fault in ~~model OOF~~the optimally oriented fault model. Additionally, the process of the stress drop is 3.8 s faster than in model RT. We can note that this difference cannot be explained by the theoretical relation in Ampuero and Mao (2017, equation 13), in which H_{max}/W is proportional to the ratio of stress drop to strength drop squared. This points to opportunities to refine that theory. In summary, a fault at an optimal angle in the interseismic sense results in a much smaller off-fault plastic yielding during earthquakes. However, due to dynamic reorientations of the fault-near stress field minor off-fault yielding still occurs.

3.4 Role of higher pressure and a thicker crust on secondary off-fault localization and main fault replacement

In order to increase the strong off-fault localization of reference model RW, with its propensity towards irregular fault pattern and unevenly spaced secondary fault branches, we increase the initial background pressure P_B of model RW by a factor of 2 (to 40 MPa). Additionally, we increase the crustal thickness T by a factor of 2, to 40 km, which is a typical value for continental crust and furthermore enhances the extent of off-fault plasticity (section 3.2.1). This model is named HPT. The rate-weakening ~~behavior~~ behaviour of the bulk is kept as in model RW to facilitate fault localization. The primary earthquake in model HPT occurs after 656.3 years, which approximately corresponds to twice the event time in model RW. The time lag is caused by the doubled P_B and the thicker crust. As the rupture propagates along the predefined main fault, secondary ruptures create localized secondary splay fault branches like in model RW. However, in contrast to model RW, the splays are sharply localized as soon as the off-fault deformation occurs (Fig. [9b]). The main fault rupture induces four dynamically rupturing secondary Riedel splays HPT1, HPT01, HPT001 and HPT0001 under the Coulomb angle. In turn, these splays induce some tertiary ruptures. Each of the dynamically created incipient faults has an extensional and a compressional side, like the main fault. Interestingly, the secondary splays in model HPT do not saturate in contrast to model RW, in which an upper bound H_{max} exists. This is caused by the higher energies of the individual ruptures due to the higher initial background pressure. Hence,

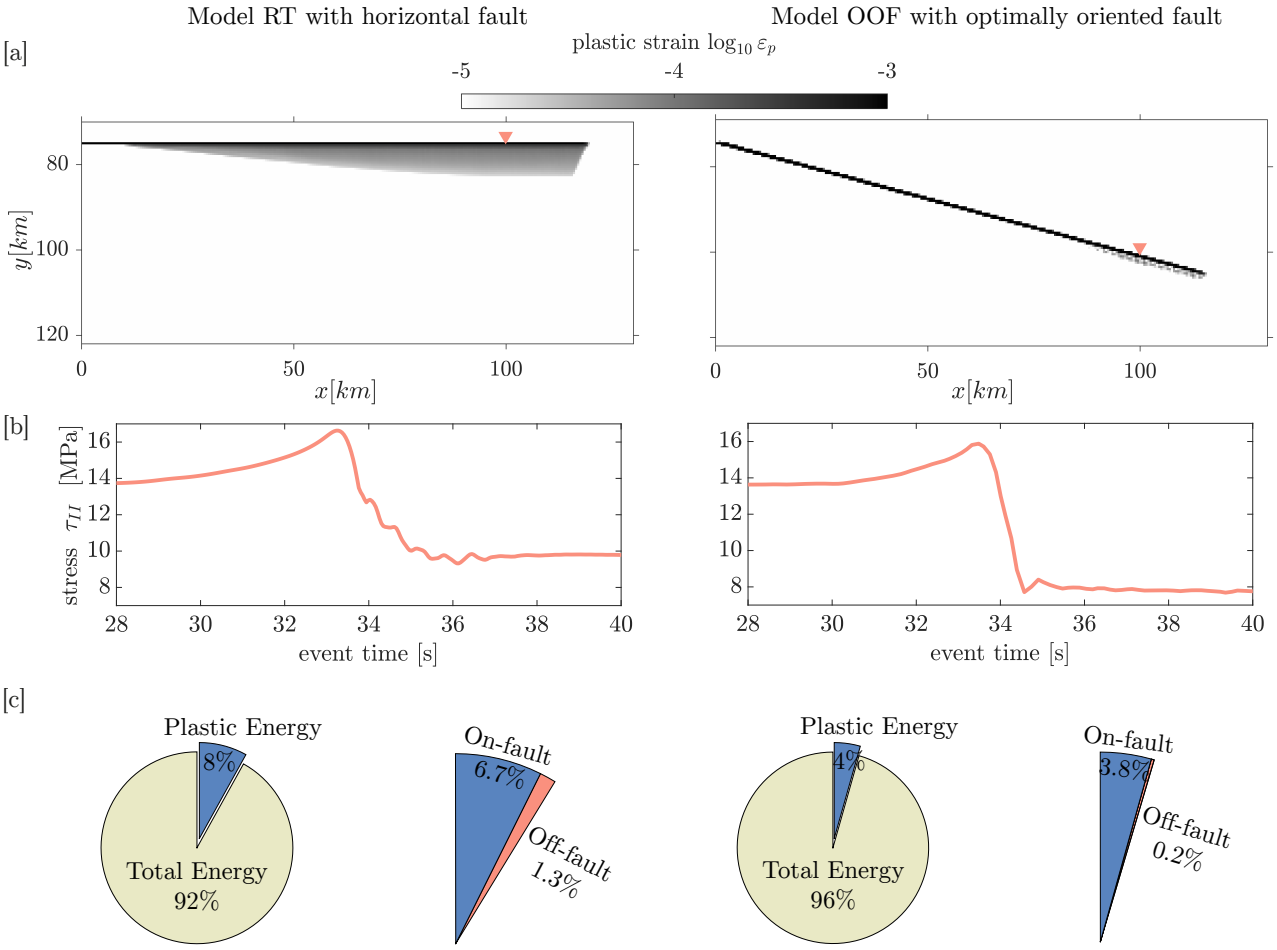

Figure 8. Comparison of plastic off-fault strain and energy between model RT and OOF (optimally oriented fault model). [a]: Accumulated plastic off-fault strain for both models in gray-scale during the first earthquake. Red triangles indicate the sample location of the stress data plotted in [b]. Panel [c] shows the ratio of the plastic energy opposed to the total energy in percentage. The plastic energy is subdivided in an on-fault (blue) and an off-fault (red) part.

this is an indication that the counteracting stresses at the base of the crust are too small to limit the extent of splay faulting in this setting. This ~~behavior~~ behaviour is particularly visible for the outermost branch HPT0001, which is most free to grow and barely interacts with other ruptures as it diverges from the predefined fault. Besides the four Riedel faults, model HPT additionally produces high-angle secondary conjugate faults. This happens even before the main fault rupture penetrates into the bulk at the tip of the predefined fault (fault strands HPT2, HPT02 and HPT002). Some of these conjugate faults extend to connect the main fault with the secondary splays and then stop growing when they intersect with the next fault strand (Fig. [9c]). The resulting fault pattern has similarities with fault structures observed in nature and their schematic interpretations (compare to Fig. [1]). Another effect of higher P_B and thicker T is that the lateral spacing between the separate branches

increases such that they become individual independent fault strands. Concurrently, these fault strands can interact with each other due to an interference of the individual local stress fields with the ones of the surrounding dynamic ruptures. This leads to irregularities in splay spacing, splay bending and abandoning of splays. We follow that a higher background pressure increases the degree of localization of the splays and affects the spacing between the splays. Additionally, the complexity in the localized off-fault deformation is increased and the combination with a higher crustal thickness enhances the spatial reach of the off-fault splays. The latter is facilitated by the rate-weakening bulk.

In the following we analyze several indications of fault and rupture interactions due to stress changes that are typically ignored in seismic cycle models. They include: (1) Rupture arrest when two sub-parallel ruptures get too close to one another. This can be observed for fault HPT001, which stops growing because the stresses on the extensional side of the subsequently forming branch HPT01 increase, get dominant and limit the compressional side stresses of HPT001. As a consequence, only extensional stresses remain at the tip of HPT001, such that the fault gets thinner on its compressional side (Fig. [9c,b]). This leads to (2) a stop in fault growth and fault abandoning. Further, fault bending (3) is observed as fault HPT02 approaches HPT0001 and the former starts to bend due to local interactions of stresses. After bending, both faults intersect (4), which causes HPT02 to terminate (5). All together, this ~~behavior~~ behaviour is well visible in the video of the HPT simulation, 19 Mb. Consequently, new interjacent branches can stop if their extensional side stress field interacts with the compressional side stress field of another rupture. This is the case when the branches of two subparallel ruptures get close to one another. In this process, the fault on the extensional side is likely to continue extending. This line of reasoning applies for a dextral fault system and is reasonable since the evolving fault structure as a total has an extensional character, which means that an extensional stress state is predominant and the extensional fault's side is ~~favored~~favoured.

The main fault rupture forms a Riedel fault HPT1 and a conjugate HPT2 like in model RW. These two faults and the secondary branch HPT01 grow until the event slip velocity drops to 8e-4 m/s after a duration of 330 s. Then, they stop growing and only the outermost splay HPT0001 continues to grow as the slip velocity again rises to the seismic range. The drop in slip velocity leads to a fault bend (red circle in Fig. [9c]). Since the outermost fault is the only active fault at the end of the simulation we infer that during the evolution of the fault network HPT a main fault change occurred. Hence, the branch HPT0001 is most ~~favorably~~ favourably oriented with the local and far-field stresses and replaces the predefined straight main fault. We refer to this dynamic process as a main fault replacement.

4 Discussion

Our results suggest that ~~the fault growthprocess in nature is best represented by bulk behavior that transitions~~ all four reference models have predominantly aseismically growing faults. A bulk rheology with constant rate-sensitivity favours a faster fault growth. In contrast, the heterogeneities introduced by a weakening of the RSF parameters L and b slow down the faulting process due to the absorption of energy by the weakening mechanism. As a consequence, the faults in the model RT that transition from rate-strengthening to rate-weakening ~~with plastic strain. Constant rate-dependent behavior in~~ can extend in alternating seismic and aseismic growth periods. Only if the region ahead of the ~~bulk results in very fast fault extension with~~

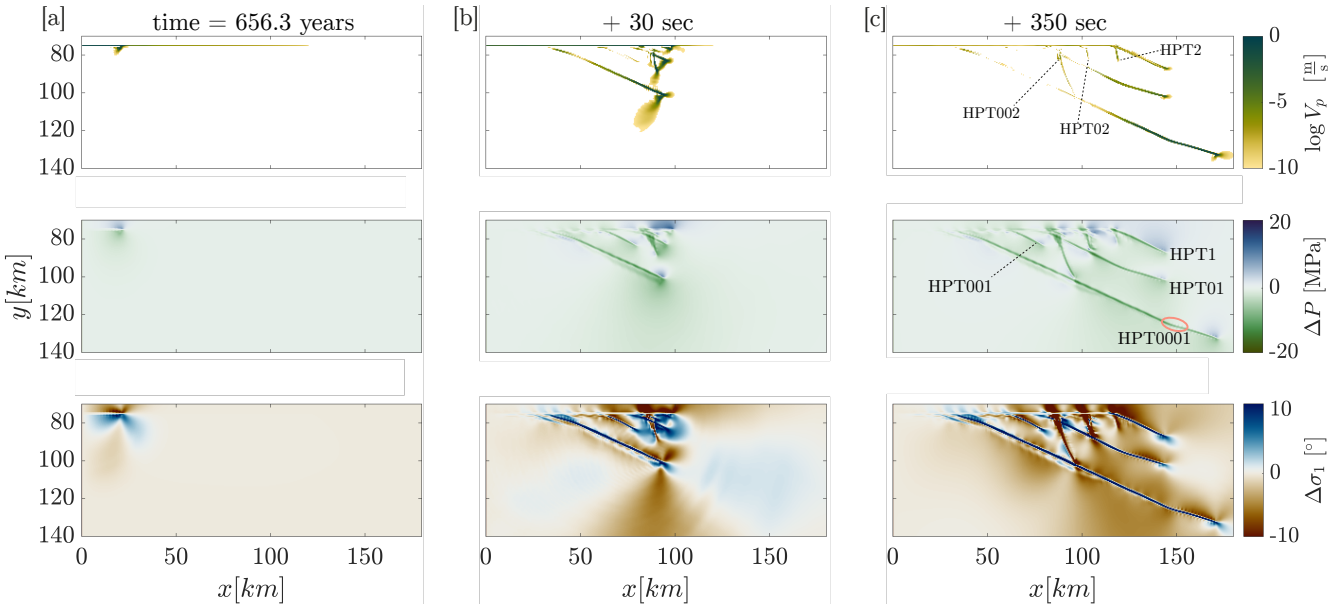

Figure 9. Model HPT with higher background pressure (P_B = 40 MPa) and increased crustal thickness (T = 40 km). Plotted are the logarithm of the slip velocity V_p, the pressure-difference ΔP between initial background pressure P_B and dynamic pressure P and the dynamic change in σ_1-orientation $\Delta \sigma_1$ for three different instants [a], [b], [c], respectively. Different fault branch names are indicated in [c]. Red circle in [c] marks the bend of branch HPT0001 due to an aseismic transition phase between two successive earthquakes.

~~unrealistic rates of up to 77 km/yr. All four reference models agree to first order with the finding that the maximum amount a fault can grow in a single earthquake that ruptures the entire fault is of~~ fault tip has experienced distinct plastic strain and L and b are altered to create a rate-weakening fault earthquakes can propagate on there. Otherwise, dynamic rupturing is hindered in the ~~order of 1% of its previous length (~~Cowie and Scholz, 1992~~). The distance a fault can grow in one event also depends on the optimality of the fault orientation and on the bulk rheology prior to the rupturing. In model RT, for example, only the first event extends the fault significantly, while the subsequent events occur after the fault orientation has already adapted to the far-field stress and extend the fault only marginally (Fig. 5).~~ intact bulk, where L is still high and b is still low and rate-strengthening, respectively. This contrast of large L and low b in the bulk rock results in intermittent seismic and aseismic growth sequences. We think this behaviour reflects the natural growth of crustal faults better than constant values of L and b, which lead to rapid fault propagation after singular earthquakes. Furthermore, evolution of L and b with strain was observed in laboratory studies (e.g. Beeler et al., 1996; Scuderi et al., 2017; Marone and Kilgore, 1993). The differences between the two end-member bulk rheologies have major implications on the dynamics and geometry of fault evolution, which are discussed in this section.

4.1 Riedel shear splays

The concept of work minimization states that new faulting starts when the active fault has become sub-optimal in the Coulomb sense, inefficient and sufficiently high amounts of strain are transferred into the surrounding rock (e.g. Cooke and Murphy,

2004; Cooke and Madden, 2014). In fact, natural faults are often ~~unfavorably~~ unfavourably oriented with respect to remotely acting stresses (e.g., Faulkner et al., 2006). In this case new, secondary faults form at acute Coulomb angles to a primary fault (Scholz et al., 2010). Several studies linked Riedel shears and Coulomb shears (e.g., Tchalenko, 1970). In all our reference models a dynamically formed Riedel fault R1 and a conjugate R2 (R') emerge at the fault tip. In the rate-weakening and rate-neutral models, Riedel faults dynamically initiate off-fault and grow during the first earthquake, which indicates that the seed fault was not optimally oriented relative to the local dynamic stresses (Fig. 4, discussed in section 4.4). Interestingly, most of the dynamically generated Riedel faults get abandoned after they form. An exception is the Riedel fault at x=105 km in model RW, which was generated during the first event and grew aseismically 0.35 years later (see video RW, 68 Mb). It is an example of a fault that is excluded from the saturating effect of the lower crustal substrate (discussed in section 4.7). A potential reason might be that the counteracting stresses of the crustal substrate caused by the primary event have ceased and the substrate is again relaxed. This means that the saturation of off-fault deformation thickness does not apply to slow growth processes whose time scale is longer than the deep relaxation time scale as was first proposed by Ampuero and Mao (2017).

We analyzed the angles of newly formed Riedel faults R1 and R2 and showed that they comply with the Mohr-Coulomb faulting theory. Earthquakes on the main fault induce a dynamic elevation of the local stress and friction coefficient and a lobe-like alteration of the stress orientations. These dynamic changes determine, via classical failure theory, greater fault angles than the typical $10° - 20°$ range reported in experimental studies (e.g., Moore et al., 1989; Tchalenko, 1970).
We reported this ~~behavior~~ behaviour already in a previous study (Preuss et al., 2019). Here, we additionally observe that the conjugate R2 responds to dynamic stresses with a decrease in β_2 due to its antithetic nature (sinistral fault in a dextral fault system). Hence, with respect to the absolute fault angle, the seismic contribution is contrary to that in a dextral fault like R1. The angle of R2 seems high, although it forms according to the classical faulting theory. A high angle was also reported in a computational study of dynamic rupture allowing for formation and growth of secondary faults during a single earthquake (Kame and Yamashita, 2003). Stress analysis of a crack loaded in mode II explains the formation of tensile fractures at the crack tip ~~(King and Sammis, 1992)~~(e.g. King and Sammis, 1992; Cooke, 1997; Poliakov et al., 2002; Rice et al., 2005).

4.2 Fault bending due to earthquakes

Owing to the differences between quasi-static and dynamic stress and strength conditions, the faults in our models reorient and bend as they alternate between aseismic and seismic growth stages. The fault angle β changes after each earthquake in all models. This ~~behavior~~ behaviour is especially well visible at the $\sim 30°$ 'big bend' of R1 at the tip of the pre-existing fault at x = 120 km (Fig. 3). Here, during the first earthquake, the pre-existing fault is severely misaligned with the locally rotated stresses. Thus, as the rupture reaches the tip of the fault and penetrates into the bulk, the fault bends under a great angle. In the following aseismic stage β decreases. This ~~behavior~~ behaviour leads to multiple smaller fault trace bends on the long-term in the case of model RT with several earthquakes (Fig. 3). This history is well traceable in the increments of fault growth in figure 5. The bends become less and less pronounced in the later stages of fault evolution because first, the contribution of seismic fault growth reduces over time; and second, the fault system tends to optimize its growth efficiency and reaches a steady state in which seismic and aseismic growth happen in the same direction (earthquakes 5,6,7 in Fig. 5). These two

reasons are interconnected. On average, the fault bends in model RT are in the order of ∼10° - 15° during fault formation, but the individual bend angles decrease over time. These values fit well within the range of 6° - 20° reported by Moore and Byerlee (1991) and the average splay bend angle of ±17° (Ando et al., 2009) for the San Andreas Fault. Additionally, these values support the statement of Preuss et al. (2019) whose stress field analysis of the Landers-Kickapoo fault suggests that an angle greater than ∼25° between two faults indicates seismic fault growth.

To summarize, our findings imply that fault bending is most likely the result of a misalignment of the pre-existing fault, which can occur also in a frictionally homogeneous medium. This fault misalignment can be strongly affected by seismically activated dynamic processes. Fault bending must not necessarily be the result of only seismic rupturing but the magnitude of bending can be strongly increased by it. Additionally, modeling shows that bending related to seismic rupture smears out over time but an overall increase of the angle of the entire fault trace can be recorded on the long-term.

4.3 Contribution of aseismic and seismic fault growth

All four reference models agree to first order with the finding that the maximum amount a fault can grow in a single earthquake that ruptures the entire fault is of the order of 1% of its previous length (Cowie and Scholz, 1992). We show that seismic growth has a visible influence on the overall fault trace angle, which is reflected in the ∼14.2° greater fault angle of the partly seismic and partly aseismic extending RT1 compared to the purely aseismic extending RS1 in the rate-strengthening model (Fig. 3). However, in general fault growth ~~in our model is mainly restricted to an aseismic contribution,~~ predominantly occurs through aseismic deformation in all four reference models, independent of the type of bulk rheological behaviour. That is because a seismic rupture only reaches the current fault tip if this part of the fault is already highly localized. This is solely the case in the first earthquake when the entire fault trace coincides with the predefined, weak, mature fault. In the subsequent earthquakes, the rupture only breaks the fault at seismic slip rates far behind the current fault tip (to the west) and the seismic rupture stops before reaching the actual fault tip (see video model RT, 116 Mb). Hence, the contribution of the seismic events is rather limited to further localizing deformation in areas of initialized distributed yielding and to increasing the overall fault trace angle than to extend the fault significantly at the tip.

4.4 On the optimality of the pre-existing fault angle

Our study shows that the amount of off-fault deformation is crucially dependent on the misalignment of the fault or, in other words, on the optimality of the angle of a predefined fault (section 3.3). For a model with an optimally oriented fault in the interseismic sense we report a 6.5-fold plastic energy decrease with respect to a fault that is parallel to the loading direction (Fig. 8). This decrease in expended energy results in significantly less plastic deformation off the main fault. The same model with an optimally oriented fault shows a 1.7-fold decrease of plastic deformation on the main fault and a stress drop increase by 149% with respect to model RT. These numbers reveal that the initial orientation of a fault subject to dynamic earthquake rupture with off-fault deformation is essential for the amount of off-fault deformation. Data from locked strike-slip faults in California confirm that stress drops are larger on faults with a greater measured Riedel angle (Moore and Byerlee, 1992). An equivalent to varying the initial fault angle is to vary the initial σ_1-direction in the simulation. A number of studies

investigated the effect of the far-field stress direction on the off-fault deformation or on the angle of dynamically rupturing secondary fault branches (Templeton and Rice, 2008; Kame et al., 2003; Rice et al., 2005; Bhat et al., 2007). The value of the slip-weakening distance was shown to regulate between more continuous along-strike damage and concentrated fracturing at fault tips (Savage and Cooke, 2010). However, these simplified studies (simple linear on-fault slip-weakening law and constant or linear slip-weakening off-fault law, simplified elastic or elastic-plastic off-fault rheology, predefined secondary fault paths, no possibility of re-nucleation of rupture and artificial event nucleation) omitted to quantify the amount of plastic off-fault strain energy related to different angles between fault and σ_1-direction.

Furthermore, we showed that the distance a fault can grow in one event also depends on the optimality of the fault orientation and on the bulk rheology prior to the rupturing. In model RT, for example, only the first event extends the fault significantly, while the subsequent events occur after the fault orientation has already adapted to the far-field stress and extend the fault only marginally (Fig. 5).

Our findings regarding the time-dependent optimality of the fault angle have implications for nature and for future dynamic rupture modeling studies. Active fault strands in nature that are surrounded by severe localized or diffuse damage zones, possibly extending far into the host rock, are strongly misaligned with the interseismic far-field stress field. This misalignment may be increased dynamically during seismic rupturing. This means that individual fault traces may reflect the local geology, structure or stress state rather than the prevailing far-field, long-term stress field and this effect would vary from segment to segment randomizing the fault pattern (Moore and Byerlee, 1989). This explains the complex nature of inter-branched crustal fault systems.

These statements are supported by model HPT, where strong local alterations of stresses lead to marked secondary rupturing and a main-fault replacement (Fig. 9). Moderate off-fault deformation close to a fault suggests that the fault is slightly misaligned in interseismic phases, which may again be amplified by dynamic reorganization of stresses. Absent or very little off-fault yielding indicate that the respective fault is well aligned with the far-field long-term stress field and dynamic rupturing on the fault has a minor effect on the off-fault stresses. Further, we showed that a higher dynamic stress drop can be taken as evidence for a well-aligned fault trace. A higher angle of the secondary splays indicates a stronger dynamic elevation of local stresses and friction due to increased slip rates, which increases the misalignment of the pre-existing fault in a dynamic sense. This statement is supported by a comparison of stably sliding and stick-slip segments in laboratory fault zones and the San Andreas fault (Moore and Byerlee, 1991). In nature it is very likely that faults adapt to the regional stress-field on the long-term (e.g., Nur et al., 1989; Swanson, 2006, 1992; Katz et al., 2004; Chester and Chester, 1998; Vermilye and Scholz, 1998).

It is noted that the typical dynamic rupture modeling setup of a 0° pre-existing fault in a constant stress field with σ_1=45° represents a very particular case. This case seems well suited to study reactivation of formerly passive faults. However, it seems less well suited to study realistic faulting processes on the long-term that are interacting with earthquakes, which alter the local stress field and friction values.

4.5 Interaction of fault branches to optimize the fault system efficiency

We found evidence for connecting fault segments, which highlights that different fault strands interact both during and between earthquakes. Dynamic interaction is versatile and pronounced in model HPT (Fig. 9 ~~and~~ video of the HPT simulation, 19 Mb). Instantaneous weakening of the local friction coefficient and an instantaneous local stress rotation at the tip of each dynamic rupture leads to complex faulting ~~behavior~~ behaviour due to an interference of the individual local stress-fields with the ones of the surrounding dynamic ruptures (section 3.4). The single main fault rupture in this model excites 10 dynamic secondary ruptures on the extensional side bulk that can arrest, bend, converge, intersect and get abandoned. This complexity is linked to spatial and temporal variations of the normal stress during and between earthquake sequences, which affect the evolving fault pattern. That ~~behavior~~ behaviour highlights the importance to include ~~a~~ both spatially and temporally varying normal stress in earthquake cycle models instead of assuming a constant normal stress or only assuming a depth dependent normal stress.

We explain the tendency that the extensional side fault of two sub-parallel faults is the ~~favored~~ favoured with the extensional stress state in a dextral fault system subject to a σ_1-direction of 45°. Supposably, a fault network in a compressive stress field ~~favors~~ favours fault growth on the compressive side in a likewise manner.

An interesting feature in model HPT is the main fault replacement (or jump). This is reflected in the singular growth and slip activity of the outermost fault branch HPT0001 at the end of the simulation. In the dynamically altered stress field this outermost fault branch is most ~~favorably~~ favourably oriented. A main fault jump was reported in southern California where the San Gabriel fault was originally the main strand of the San Andreas fault, but was replaced at about 4 Ma (Moore and Byerlee, 1991). Faults that are ~~unfavorably~~ unfavourably oriented for large amounts of slip will be replaced by progressively better oriented faults ~~(Moore and Byerlee, 1989)~~(e.g. Moore and Byerlee, 1989).

Fault branch interaction occurs also on the long-term when the stress fields of approaching fault strands start to interfere (manifest in a seismically initiated incipient connection between RT1 and RT2 at x∼140 km in Fig. 3). Seemingly, the fault system intends to increase its efficiency by decreasing the fault complexity on the long-term due to fault interaction which can lead to abandoning of abundant fault strands. This is another indication, apart from the previously discussed one, that the fault optimizes its growth efficiency and aims at reaching a steady state on the long-term in which seismic and aseismic growth preferentially happen in the same direction.

4.6 Wing crack transition and relation to normal and reverse faults in the Anatolian Fault system

The decreasing strike angle of fault RT2 brings another aspect with it. The fault RT2 is initially formed at the typical angle of a conjugate Riedel fault (R') and agrees with the standard Mohr-Coulomb failure criterion (Fig. 4). The predictions during the earthquake agree very well with the angles determined in laboratory experiments (Tchalenko, 1970). In the subsequent aseismic stage the angle of the conjugate RT2 starts to decrease. This ~~behavior~~ behaviour leads to a bending of RT2 on the long-term (Fig. 3, video RT, 116 Mb). The conjugate angle decreases from an initial value of ~~72~~75° to an angle of 56° at the end of the simulation. A tension fracture or wing crack forms perpendicular to the orientation of the minimum principal stress direction (Dooley and Schreurs, 2012). In our 2.5-D plane strain model this implies a formation parallel to the σ_1-

direction. One could argue that the fault RT2 is undergoing a transition phase from a conjugate Riedel fault to a tension fracture. Before this transition is completed the simulation is stopped because RT1 has reached the eastern model boundary. Two more characteristics amplify this argument. Firstly, the counterclockwise bending ~~behavior~~ behaviour of RT2 corresponds to the one of a wing crack (=tension fracture) in laboratory experiments (illustrated in Fig. [1d], ~~(e.g. Willemse and Pollard, 1998)~~ (e.g. Cooke, 1997; Willemse and Pollard, 1998)). Secondly, we record a significant amount of opening for RT2, which varies in the range of 50% - 100% compared to the shear component of RT2. This is another similarity to a classical tension fracture, which is typically an opening mode crack (Willemse and Pollard, 1998). Nonetheless, the dominant shear component alludes to a transition or an approximation to a wing crack rather than the development of a classical wing crack.

Such classical wing cracks are typically found in laboratory experiments and as subsidiary cracks in nature (e.g. Lee et al., 2016; Birren and Reber, 2019; Mutlu and Pollard, 2008; Willemse and Pollard, 1998). In the following we briefly attempt to link our model observations with the theory of wing cracks and normal and reverse faults in nature. Similarities between wing cracks and normal faults at a larger scale were reported before (e.g. Mutlu and Pollard, 2008). A modeling study of the Anatolian Fault system linked mode I wing crack formation to large scale mode I failure representing dyke, normal fault or rift formation (Hubert-Ferrari et al., 2003). Their Coulomb shear failure map predicts left-lateral optimum fault formation in areas of increased tensile stresses compatible with the creation of the East Anatolian Fault. Furthermore, their associated left-lateral optimum faults coincide well with mapped normal faults branching off under steep angles from the main North Anatolian strike-slip fault (see supplementary material of Perrin et al., 2016b). Many of such normal faults and also branching thrust faults are found in the Cinarcik Basin, the Central High area south of Büyükçekmece and the Central Basin south of Marmaraereğlisi (Le Pichon et al., 2003). A perfect example is the Gölcük normal fault just west of the Izmit fault that is oriented at 46° to the main North Anatolian fault trace (Barka et al., 2002) and also small-scale normal faults with similar trends and 45° oblique to the master fault (Alpar and Yaltirak, 2002). Thus, transtensional and normal faulting that are located near pull-apart basins in the North Anatolian fault system (Ickrath et al., 2015) are geometrically very similar to lab-scale opening wing-cracks and the fault RT2 of our simulation. They evolve in a tension-gash just like wing-cracks (Sengör et al., 2004) and RT2 develops in the direction of such a tension-gash. Additionally, their transtensional nature is reflected in the shear- and opening-component of RT2, which is a necessary prerequisite for extensional faulting. Another great example of normal and thrust faults bordering an advancing strike-slip fault is the Altyn Tagh fault (see map in Perrin et al., 2016b). Some of the branching splays in this example are marked by the same bending ~~behavior~~ behaviour as RT2 farther away from the main fault.

4.7 Width of the off-fault fan

In section 3.2.1 we showed that the implementation of the 2.5-D approximation has a limiting effect on the width of the dynamically created plastic fan off the main fault, which is observed for the width of the inner damage zone in 3-D numerical models and in nature (Ampuero and Mao, 2017; Savage and Brodsky, 2011; Perrin et al., 2016b). This limiting effect is controlled by the transition from a crack-like to a pulse-like rupture shown in figure 6, which is evoked by counteracting stresses in response to the sudden excitement of earthquake forces at the surface of the relaxed lower crustal substrate. The

width of the ~~fan is~~ plastic fan in our models is larger than that seen in observations from Savage and Brodsky (2011). This difference is related to the non-optimally oriented fault of the reference model, which was discussed in section 4.4 and which is compared to an optimally oriented fault with a significantly lower width of the plastic yielding fan in figure 8. Furthermore, the plane strain assumption in our 2.5-D model assumes a constant thickness of the seismogenic fault with depth-constant rate-weakening behavior, which favours a larger width of the plastic yielding fan generated during earthquakes if it is compared to a natural fault which typically has alternating rate-weakening and rate-strengthening patches. Additionally, in our model the width of the fan is controlled by several parameters, of which the thickness of the elastic layer T on top of the visco-elastic half-space has the greatest impact. ~~Too high~~ Higher values of $(a-b)$ ~~and too high and too~~ as well as high and low initial bulk host rock state variable values θ_{hr} decrease the fan width significantly. If $(a-b)$ decreases towards 0, the fan width approaches the fan width of the rate-neutral model for which $(a-b)=0$. A change of slip velocity due to the variation of one parameter does not affect the plastic-fan width (Fig. 7). Another effect of the visco-elastic lower crustal substrate is the delayed onset of the first dynamic earthquake due to the viscous contribution of the lower layer compared to a pure 2-D simulation in which the crust is infinitely thick.

4.8 ~~Modeling~~ Comparison to previous publications, modeling limitations and future work

The natural faulting process is a three dimensional process. Compared to previous studies that applied the STM-code we here approach three-dimensionality by a 2.5-D approximation. We thus obtain a finiteness of the seismogenic depth that limits the stress concentration at the fault tip, which in turn limits the spatial extent of plasticity outside the main fault (Ampuero and Mao, 2017). However, this approximation assumes a simple linearly elastic crust and computes the thickness averaged stresses in it due to traveling rupture zones. This approximation does not actually account for the third dimension and neglects parameter variations with depth as well as a possible change of the fault dip angle with depth. In this study faults are always vertical in a plane-strain sense, cutting through the entire upper crustal layer. This implies that faults in our models can not initiate at depth and link from an early set of echelon faults that propagate upwards as shown by analogue experiments. Further, the simulations exclude a temperature-dependent rheology that would imply rheology changes with depth. The presented comparison of rate-strengthening, rate-neutral, rate-weakening and a transition case between them can be seen as an insightful improvement compared to our previous study in which we only uses a rate-weakening bulk material (Preuss et al., 2019). In particular it represents an improvement because it simulates ~~behavior~~ behaviour observed in the laboratory. Here, we presented changes of frictional parameters L and $(a-b)$ with plastic strain. Additionally, we run test models in which we weakened a instead of b keeping the overall $(a-b)$ constant. Further, we tested a simultaneous weakening of a and b keeping $(a-b)$ again constant. These different weakening scenarios do not change the ~~behavior~~ behaviour of the model. However, changes of other frictional parameters or material parameters (e.g., shear modulus) with plastic strain are not taken into account in our simulations despite they can be expected in natural fault systems. Our model is a simplification in that it ignores anisotropy, poroelasticity, or dilatant volume changes, which are typically observed in natural faults (e.g., Woodcock et al., 2007; Brace et al., 1966; Peacock and Sanderson, 1992; Rawling et al., 2002). Our choice of parameters results in a Poisson's ratio of 0.125. Such a relatively low Poisson's ratio is on the lower end of values for rocks, but still common for a wide range of rock

types as for example shown in Gercek (2007). To illustrate the impact of different Poisson's ratios we have tested a range of different shear moduli resulting in varying Poisson's ratios. These tests have shown that the main messages of our manuscript are not influenced by changes in the Poisson's ratio. In our previous work we discussed the need for an alternative invariant continuum-based rate- and state-dependent friction formulation for fault width W. The result of using the here proposed slip-velocity-dependent heuristic fault-width formulation is that both the fault angle and the temporal onset of the earthquake converge with grid size at a resolution of 250 m (appendix A). Due to computational time reasons all our reference models had to be run with a resolution of 500 m, however. With respect to the note in section 4.4 of Preuss et al. (2019) we here want to add that our proposed heuristic fix needs further research including the comparison to analog models to test and further refine the continuum-based constitutive relationship describing self-consistently both localization toward a fault and deformation within the fault.

5 Conclusions

In this study we simulated the spatio-temporal evolution of a complex strike-slip fault system subjected to repeated earthquake ruptures. We applied an invariant rate- and state-dependent friction formulation framework that allows for the spontaneous growth and evolution of a fault. This STM-RSF framework was extended with a 2.5-D approximation, a new dynamically adapting slip-velocity-dependent fault-width formulation and a plastic-strain-weakening mechanism of bulk parameters inspired by laboratory experiments. With this advanced model we present different possibilities of how a strike-slip fault grows due to (a)seismic processes in different host rock rheologies of which the end-member cases are bulk-velocity-weakening and bulk-velocity-strengthening. This work focuses on three main aspects: 1) It discriminates between the conditions leading to distributed or localized dynamic off-fault deformation and the saturation of the plastic zone width. Our models distinguish between off-fault deformation geometries observed in nature (Fig. 1). 2) This study analyzes distinct ~~extension~~ propagation styles of the main fault leading to a complex interactive fault network with bends caused by differences in angle between seismic and aseismic segments. The different fault branches are successfully linked to the Mohr-Coulomb faulting criterion. The development of Riedel shear faults and their conjugates is caused by dynamic stress field effects and also explained by the theoretical faulting criterion. 3) Ultimately, our study demonstrates that the amount of plastic off-fault deformation crucially depends on both the initial fault orientation with respect to the far-field stresses but also on the dynamic optimality of the fault angle in relation to local stresses. The optimality of fault alignment in a stress field is time-dependent and depends on local variations of rotating stress orientations.

Additionally, we found that under the wide range of conditions explored the contribution of seismic fault growth is limited compared to the aseismic contribution. Earthquakes are rather leading to a greater localization in areas of distributed deformation close to the fault tip. Nevertheless, the overall fault angle of a fault that extends by combined aseismic and seismic growth is 14.2° greater than the fault angle of a purely aseismically growing fault. Further, the earthquakes evoke small segment bends in the order of $\sim$10° - 15° along a fault trace. However, to some extent these bends get smeared out over time as the fault straightens gradually.

With respect to fault branch and rupture interactions we reported rupture arrest, fault bending, fault convergence and intersection, arrest of fault growth and fault strand abandoning. Fault interaction was observed on the long-term and during coseismic events. In an extensional fault setting the extensional side fault of two sub-parallel faults is the ~~favored~~ favoured one and likely to continue. The dynamic rotation of stresses can lead to a reorientation of stresses, which might result in the severe misalignment of the former main fault. This will lead to a replacement of the main fault trace and a jump of fault activity. Thus, fault systems tend to optimize their efficiency by adapting to changing conditions. We additionally found that fault systems optimize their growth efficiency by progressively ~~favoring~~ favouring similar growth directions for seismic and aseismic growth. With our work we provide the basis for simulations and analyses of complex evolving fault networks subject to long-term and short-term dynamics. The approach we presented has potential to be applied to a more realistic fault map in a future study.

Code and data availability. The code is available upon request to T. Gerya (taras.gerya@erdw.ethz.ch). With this code the four reference models can be rerun. Figures 3 - 6 of this paper can thus be reproduced.

Video supplement. The repository cited in the references (Preuss et al., 2020) contains five videos showing the temporal evolution of the four reference models and model HPT, which are all discussed in the main text.

Appendix A: Test of the slip-velocity-dependent fault-width formulation

We tested the new slip-velocity-dependent fault-width formulation (equation 15) using 4 different resolutions (Δx = 125 m, 250 m, 500 m and 1000 m). The used model setup is the one from Preuss et al. (2019) because in it faults are completely free to start growing from the center of the model without any pre-defined fault line but a small elliptical defect. In this model, faults grow both aseismically and seismically, however, under a different angle. This is considered in the convergence analysis, which shows that both seismic and aseismic fault angles converge with grid size (Fig. [A1 a,b]). Also, the time of the earthquake converges with grid size in similar manner (Fig. [A1 d]). We note that the model with the lowest resolution has a temporal onset of the event, which is only 0.86 years off from the highest resolved model. In conclusion and based on the convergence analysis of the new slip-velocity-dependent fault-width formulation, the authors choose to apply the second finest resolution, Δx = 250 m, for all model runs. This decision is mainly based on the fact that the highest variation is found in the seismic fault angles, while the seismic relative fault angle α as well as the seismic absolute fault angle β converge for $\Delta x \leq 250$ m. The aseismic fault angles and the temporal onset of the earthquake start to converge before, i.e. for $\Delta x \geq 250$ m.

Author contributions. Simon Preuss designed the study, implemented and tested the 2.5-D approximation and the dynamically adaptive measure of fault width, designed the model setup, decided the parameter space, ran the simulations, gathered and interpreted the results, wrote the manuscript and organized the submission process. Jean Paul Ampuero provided the initial idea to use the 2.5-D generalized Elsasser approach, helped clarifying the results and improved the manuscript. Taras Gerya provided the initial idea and tests of the dynamically adaptive measure of fault width, assisted in formulating the 2.5-D approximation for STM-RSF and helped to design the initial model setup. Ylona van Dinther helped clarifying the results and improved the manuscript.

Competing interests. There are no competing interests.

Acknowledgements. ~~The repository cited in the references (~~Preuss et al.~~, 2020) contains four executables, with which the four reference models can be rerun. Figures 3 - 6 of this paper can thus be reproduced. Pending further notice the following link will lead to a temporary repository, in case the permanent repository is not yet accessible: .~~ This project acknowledges support through the SNF research grant 200021_182069. J.P.A. was supported by the French National Research Agency (ANR) through project FAULTS_R_GEMS (Grant ANR-17-CE31-0008) and Investments-in-the-Future project UCAJEDI (Grant ANR-15-IDEX-01). We thank Robert Herrendörfer for providing the STM-RSF code. We additionally thank André Niemeijer for a discussion on rate-and-state friction parameters for the bulk and Jianye Chen for giving very useful comments on the slip-velocity-dependent fault-width formulation. For constructive comments and discussions we thank the STM-group at ETH Zurich. Numerical simulations were performed on ETH clusters Leonhard and Euler. Perceptually uniform color maps are used in this study to prevent visual distortion of the data (Crameri, 2018).

References

Alpar, B. and Yaltirak, C.: Characteristic features of the North Anatolian Fault in the eastern Marmara region and its tectonic evolution, Marine Geology, 190, 329–350, https://doi.org/10.1016/S0025-3227(02)00353-5, 2002.

Ampuero, J. P. and Mao, X.: Upper limit on damage zone thickness controlled by seismogenic depth, Fault Zone Dynamic Processes: Evolution of Fault Properties During Seismic Rupture, 227, 243, https://doi.org/10.1002/9781119156895.ch13, 2017.

Ando, R., Shaw, B. E., and Scholz, C. H.: Quantifying natural fault geometry: Statistical of splay fault angles, Bulletin of the Seismological Society of America, 99, 389–395, https://doi.org/10.1785/0120080942, 2009.

Andrews, D. J.: Rupture Propagation With Finite Stress in Antiplane Strain., Journal of Geophysical Research, 81, 3575–3582, https://doi.org/10.1029/JB081i020p03575, https://agupubs.onlinelibrary.wiley.com/doi/abs/10.1029/JB081i020p03575, 1976.

Andrews, D. J.: Rupture dynamics with energy loss outside the slip zone, Journal of Geophysical Research: Solid Earth, 110, 1–14, https://doi.org/10.1029/2004JB003191, 2005.

Ashby, M. F. and Sammis, C. G.: The damage mechanics of brittle solids in compression, Pure and Applied Geophysics PAGEOPH, 133, 489–521, https://doi.org/10.1007/BF00878002, 1990.

Aydin, A. and Berryman, J. G.: Analysis of the growth of strike-slip faults using effective medium theory, Journal of Structural Geology, 32, 1629–1642, https://doi.org/10.1016/j.jsg.2009.11.007, http://dx.doi.org/10.1016/j.jsg.2009.11.007, 2010.

Barka, A., Akyüz, H. S., Altunel, E., Sunal, G., Çakir, Z., Dikbas, A., Yerli, B., Armijo, R., Meyer, B., De Chabalier, J. B., Rockwell, T., Dolan, J. R., Hartleb, R., Dawson, T., Christofferson, S., Tucker, A., Fumal, T., Langridge, R., Stenner, H., Lettis, W., Bachhuber, J., and Page, W.: The surface rupture and slip distribution of the 17 August 1999 Izmit earthquake (M 7.4), North Anatolian fault, Bulletin of the Seismological Society of America, 92, 43–60, https://doi.org/10.1785/0120000841, 2002.

Barth, N. C., Boulton, C., Carpenter, B. M., Batt, G. E., and Toy, V. G.: Slip localization on the southern Alpine Fault , New Zealand, Tectonics, 32, 620–640, https://doi.org/10.1002/tect.20041, 2013.

Beeler, N. M., Tullis, T. E., Blanpied, M. L., and Weeks, J. D.: Frictional behavior of large displacement experimental faults, Journal of Geophysical Research: Solid Earth, 101, 8697–8715, https://doi.org/10.1029/96JB00411, http://doi.wiley.com/10.1029/96JB00411, 1996.

Bhat, H. S., Dmowska, R., Rice, J. R., and Kame, N.: Dynamic slip transfer from the Denali to totschunda faults, Alaska: Testing theory for fault branching, Bulletin of the Seismological Society of America, 94, 202–213, https://doi.org/10.1785/0120040601, 2004.

Bhat, H. S., Olives, M., Dmowska, R., and Rice, J. R.: Role of fault branches in earthquake rupture dynamics, Journal of Geophysical Research: Solid Earth, 112, 1–16, https://doi.org/10.1029/2007JB005027, 2007.

Bhat, H. S., Rosakis, A. J., and Sammis, C. G.: A Micromechanics Based Constitutive Model for Brittle Failure at High Strain Rates, Journal of Applied Mechanics, 79, 031 016, https://doi.org/10.1115/1.4005897, http://appliedmechanics.asmedigitalcollection.asme.org/article.aspx?articleid=1421505, 2012.

Birren, T. and Reber, J. E.: The Impact of Rheology on the Transition From Stick-Slip to Creep in a Semibrittle Analog, Journal of Geophysical Research: Solid Earth, 124, 3144–3154, https://doi.org/10.1029/2018JB016914, 2019.

Brace, W. F., Paulding, B. W., and Scholz, C.: Dilatancy in the fracture of crystalline rocks, Journal of Geophysical Research, 71, 3939–3953, https://doi.org/10.1029/jz071i016p03939, 1966.

Brantut, N., Schubnel, A., Rouzaud, J., Brunet, F., and Shimamoto, T.: High-velocity frictional properties of a clay-bearing fault gouge and implications for earthquake mechanics, Journal of Geophysical Research, 113, 1–18, https://doi.org/10.1029/2007JB005551, 2008.

Buiter, S. J. H., Babeyko, A. Y., Ellis, S., Gerya, T. V., Kaus, B. J., Kellner, A., Schreurs, G., and Yamada, Y.: The numerical sandbox: Comparison of model results for a shortening and an extension experiment, Geological Society Special Publication, 253, 29–64, https://doi.org/10.1144/GSL.SP.2006.253.01.02, 2006.

Cappa, F., Perrin, C., Manighetti, I., and Delor, E.: Off-fault long-term damage: A condition to account for generic, triangular earthquake slip profiles, Geochemistry, Geophysics, Geosystems, 15, 1476–1493, https://doi.org/https://doi.org/10.1002/2013GC005182, 2014.

Chen, J., Niemeijer, A. R., and Spiers, C. J.: Microphysically Derived Expressions for Rate-and-State Friction Parameters, a, b, and Dc, Journal of Geophysical Research: Solid Earth, 122, 9627–9657, https://doi.org/10.1002/2017JB014226, 2017.

Chester, F. M. and Chester, J. S.: Ultracataclasite structure and friction processes of the Punchbowl fault, San Andreas system, California, Tectonophysics, 295, 199–221, https://doi.org/10.1016/S0040-1951(98)00121-8, 1998.

Chester, F. M., Evans, J. P., and Biegel, R. L.: Internal structure and weakening mechanisms of the San Andreas Fault, Journal of Geodynamics, 98, 771–786, https://doi.org/https://doi.org/10.1029/92JB01866, 1993.

Collettini, C., Carpenter, B. M., Viti, C., Cruciani, F., Mollo, S., and Tesei, T.: Fault structure and slip localization in carbonate-bearing normal faults : An example from the Northern Apennines of Italy, Journal of Structural Geology, 67, 154–166, https://doi.org/10.1016/j.jsg.2014.07.017, http://dx.doi.org/10.1016/j.jsg.2014.07.017, 2014.

Cooke, M.: Fracture localization along faults with spatially varying friction, Journal of Geophysical Research, 102, 22 425–22 434, 1997.

Cooke, M. L. and Madden, E. H.: Is the Earth Lazy? A review of work minimization in fault evolution, Journal of Structural Geology, 66, 334–346, https://doi.org/10.1016/j.jsg.2014.05.004, http://dx.doi.org/10.1016/j.jsg.2014.05.004, 2014.

Cooke, M. L. and Murphy, S.: Assessing the work budget and efficiency of fault systems using mechanical models, Journal of Geophysical Research: Solid Earth, 109, 1–13, https://doi.org/10.1029/2004JB002968, 2004.

Cowie, P. A. and Scholz, C. H.: Growth of faults by accumulation of seismic slip, Journal of Geophysical Research, 97, 11 085, https://doi.org/10.1029/92JB00586, http://doi.wiley.com/10.1029/92JB00586, 1992.

Crameri, F.: Geodynamic diagnostics, scientific visualisation and StagLab 3.0, Geoscientific Model Development, 11, 2541–2562, https://doi.org/10.5194/gmd-11-2541-2018, 2018.

Dieterich, J. H.: Constitutive properties of faults with simulated gouge, Geophysical Monograph Series, 24, 103–120, https://doi.org/10.1029/GM024p0103, http://doi.wiley.com/10.1029/GM024p0103, 1981.

Dooley, T. P. and Schreurs, G.: Analogue modelling of intraplate strike-slip tectonics: A review and new experimental results, Tectonophysics, 574-575, 1–71, https://doi.org/10.1016/j.tecto.2012.05.030, http://dx.doi.org/10.1016/j.tecto.2012.05.030, 2012.

Drucker, D. C. and Prager, W.: Soil mechanics and plastic analysis or limit design, Quarterly of Applied Mathematics, 10, 157–165, https://doi.org/10.1090/qam/48291, http://www.ams.org/qam/1952-10-02/S0033-569X-1952-48291-2/, 1952.

Erdogan, F. and Sih, G. C.: On the Crack Extension in Plates Under Plane Loading and Transverse Shear, Journal of Basic Engineering, 85, 519, https://doi.org/10.1115/1.3656897, http://fluidsengineering.asmedigitalcollection.asme.org/article.aspx?articleid=1431534, 1963.

Erickson, B. A., Dunham, E. M., and Khosravifar, A.: A finite difference method for off-fault plasticity throughout the earthquake cycle, Journal of the Mechanics and Physics of Solids, 109, 50–77, https://doi.org/10.1016/j.jmps.2017.08.002, http://dx.doi.org/10.1016/j.jmps.2017.08.002, 2017.

Fang, Z. and Dunham, E. M.: Additional shear resistance from fault roughness and stress levels on geometrically complex faults, Journal of Geophysical Research: Solid Earth, 118, 3642–3654, https://doi.org/10.1002/jgrb.50262, 2013.

Faulkner, D. R., Mitchell, T. M., Healy, D., and Heap, M. J.: Slip on 'weak' faults by the rotation of regional stress in the fracture damage zone, Nature, 444, 922–925, https://doi.org/10.1038/nature05353, 2006.

Faulkner, D. R., Mitchell, T. M., Jensen, E., and Cembrano, J.: Scaling of fault damage zones with displacement and the implications for fault growth processes, Journal of Geophysical Research: Solid Earth, 116, 1–11, https://doi.org/10.1029/2010JB007788, 2011.

Gabriel, A. A., Ampuero, J. P., Dalguer, L. A., and Mai, P. M.: Source properties of dynamic rupture pulses with off-fault plasticity, Journal of Geophysical Research: Solid Earth, 118, 4117–4126, https://doi.org/10.1002/jgrb.50213, 2013.

Gercek, H.: Poisson's ratio values for rocks, International Journal of Rock Mechanics and Mining Sciences, 44, 1–13, https://doi.org/10.1016/j.ijrmms.2006.04.011, 2007.

Gerya, T. V. and Yuen, D. A.: Characteristics-based marker-in-cell method with conservative finite-differences schemes for modeling geological flows with strongly variable transport properties, Physics of the Earth and Planetary Interiors, 140, 293–318, https://doi.org/10.1016/j.pepi.2003.09.006, 2003.

Gerya, T. V. and Yuen, D. A.: Robust characteristics method for modelling multiphase visco-elasto-plastic thermo-mechanical problems, Physics of the Earth and Planetary Interiors, 163, 83–105, https://doi.org/10.1016/j.pepi.2007.04.015, http://linkinghub.elsevier.com/retrieve/pii/S0031920107000969, 2007.

Han, R., Hirose, T., and Shimamoto, T.: Strong velocity weakening and powder lubrication of simulated carbonate faults at seismic slip rates, Journal of Geophysical Research, 115, https://doi.org/10.1029/2008JB006136, 2010.

Hatem, A. E., Cooke, M. L., and Toeneboehn, K.: Strain localization and evolving kinematic efficiency of initiating strike-slip faults within wet kaolin experiments, Journal of Structural Geology, 101, 96–108, https://doi.org/10.1016/j.jsg.2017.06.011, http://dx.doi.org/10.1016/j.jsg.2017.06.011, 2017.

Herrendörfer, R., Gerya, T. V., and van Dinther, Y.: An Invariant Rate- and State-Dependent Friction Formulation for Viscoeastoplastic Earthquake Cycle Simulations, Journal of Geophysical Research: Solid Earth, 123, 5018–5051, https://doi.org/10.1029/2017JB015225, 2018.

Hobbs, B. E., Mühlhaus, H. B., and Ord, A.: Instability, softening and localization of deformation, Geological Society Special Publication, 54, 143–165, https://doi.org/10.1144/GSL.SP.1990.054.01.15, 1990.

Hubert-Ferrari, A., King, G., Manighetti, I., Armijo, R., Meyer, B., and Tapponnier, P.: Long-term elasticity in the continental lithosphere; modelling the Aden Ridge propagation and the Anatolian extrusion process, Geophysical Journal International, 153, 111–132, https://doi.org/10.1046/j.1365-246X.2003.01872.x, 2003.

Ickrath, M., Bohnhoff, M., Dresen, G., Martínez-Garzón, P., Bulut, F., Kwiatek, G., and Germer, O.: Detailed analysis of spatiotemporal variations of the stress field orientation along the Izmit-Düzce rupture in NW Turkey from inversion of first-motion polarity data, Geophysical Journal International, 202, 2120–2132, https://doi.org/10.1093/gji/ggv273, 2015.

Ikari, M. J.: Principal slip zones : Precursors but not recorders of earthquake slip, Geology, 43, 955–958, https://doi.org/10.1130/G37028.1, 2015.

Jenkins, J. T.: Localization in granylar materials, Applied Mechanics Reviews, 43, 194–195, https://doi.org/doi:10.1115/1.3120803, 1990.

Jolivet, R., Lasserre, C., Doin, M. P., Peltzer, G., Avouac, J. P., Sun, J., and Dailu, R.: Spatio-temporal evolution of aseismic slip along the Haiyuan fault, China: Implications for fault frictional properties, Earth and Planetary Science Letters, 377-378, 23–33, https://doi.org/10.1016/j.epsl.2013.07.020, http://dx.doi.org/10.1016/j.epsl.2013.07.020, 2013.

Jolivet, R., Simons, M., Agram, P. S., Duputel, Z., and Shen, Z. K.: Aseismic slip and seismogenic coupling along the central San Andreas Fault, Geophysical Research Letters, 42, 297–306, https://doi.org/10.1002/2014GL062222, 2015.

Kame, N. and Yamashita, T.: Dynamic branching, arresting of rupture and the seismic wave radiation in self-chosen crack path modelling, Geophysical Journal International, 155, 1042–1050, https://doi.org/10.1111/j.1365-246X.2003.02113.x, https://academic.oup.com/gji/article/155/3/1042/628048, 2003.

Kame, N., Rice, J. R., and Dmowska, R.: Effects of prestress state and rupture velocity on dynamic fault branching, Journal of Geophysical Research: Solid Earth, 108, 1–21, https://doi.org/10.1029/2002JB002189, http://doi.wiley.com/10.1029/2002JB002189, 2003.

Katz, Y., Weinberger, R., and Aydin, A.: Geometry and kinematic evolution of Riedel shear structures, Capitol Reef National Park, Utah, Journal of Structural Geology, 26, 491–501, https://doi.org/10.1016/j.jsg.2003.08.003, 2004.

Kim, Y. S., Peacock, D. C. P., and Sanderson, D. J.: Fault damage zones, Journal of Structural Geology, 26, 503–517, https://doi.org/10.1016/j.jsg.2003.08.002, 2004.

King, G. C. and Sammis, C. G.: The mechanisms of finite brittle strain, Pure and Applied Geophysics PAGEOPH, 138, 611–640, https://doi.org/10.1007/BF00876341, 1992.

Lapusta, N. and Barbot, S.: Models of earthquakes and aseismic slip based on laboratory-derived rate and state friction laws, vol. 661, Research Signpost, Kerala, India, 2012.

Lapusta, N., Rice, J. R., Ben-Zion, Y., and Zheng, G.: Elastodynamic analysis for slow tectonic loading with spontaneous rupture episodes on faults with rate- and state-dependent friction, Journal of Geophysical Research, 105, 23 765, https://doi.org/10.1029/2000JB900250, 2000.

Lavier, L. L., Buck, W. R., and Poliakov, A. N. B.: Factors controlling normal fault offset in an ideal brittle layer, Journal of Geophysical Research, 105, 23 431, https://doi.org/10.1029/2000JB900108, http://www.agu.org/pubs/crossref/2000/2000JB900108.shtml, 2000.

Le Pichon, X., Chamot-Rooke, N., Rangin, C., and Sengör, A. M. C.: The North Anatolian fault in the Sea of Marmara, Journal of Geophysical Research: Solid Earth, 108, 1–20, https://doi.org/10.1029/2002jb001862, 2003.

Lee, S., Reber, J. E., Hayman, N. W., and Wheeler, M. F.: Investigation of wing crack formation with a combined phase-field and experimental approach, Geophysical Research Letters, 43, 7946–7952, https://doi.org/10.1002/2016GL069979, 2016.

Lehner, F. K., Li, V. C., and Rice, J. R.: Stress Diffusion Along Rupturing Plate Boundaries, Journal of Geophysical Research, 86, 6155–6169, 1981.

Lindsey, E. O. and Fialko, Y.: Geodetic constraints on frictional properties and earthquake hazard in the Imperial Valley, Southern California, Journal of Geophysical Research B: Solid Earth, 121, 1097–1113, https://doi.org/10.1002/2015JB012516, 2016.

Logan., J., Friedman, M., Higgs, M., Dengo, C., and Shimamoto, T.: Experimental studies of Simulated gouge and their application to studies of natural fault zones, U.S. Geo!. Survey, Menlo Park, CA., Analysis o, 305–343, 1979.

Logan, J. M. and Rauenzahn, A. K.: Frictional dependence of gouge mixtures of quartz and montmorillonite on velocity , composition and fabric, Tectonophysics, 144, 87–108, https://doi.org/https://doi.org/10.1016/0040-1951(87)90010-2, 1987.

Logan, J. M., Dengo, C. A., Higgs, N. G., and Wang, Z. Z.: Fabrics of Experimental Fault Zones: Their Development and Relationship to Mechanical Behavior, vol. 51, Elsevier, https://doi.org/10.1016/S0074-6142(08)62814-4, 1992.

Manighetti, I., King, G., and Sammis, C. G.: The role of off-fault damage in the evolution of normal faults, Earth and Planetary Science Letters, 217, 399–408, https://doi.org/10.1016/S0012-821X(03)00601-0, 2004.

Marone, C. and Kilgore, B.: Scaling of the critical slip distance for seismic faulting with shear strain in fault zones, Nature, 362, 618–621, https://doi.org/10.1038/362618a0, http://www.nature.com/doifinder/10.1038/362618a0, 1993.

Marone, C., Hobbs, B. E., and Ord, A.: Coulomb constitutive laws for friction: Contrasts in frictional behavior for distributed and localized shear, Pure and Applied Geophysics PAGEOPH, 139, 195–214, https://doi.org/10.1007/BF00876327, 1992.

Meyer, S. E., Kaus, B., and Passchier, C.: Development of branching brittle and ductile shear zones: A numerical study, Geochemistry, Geophysics, Geosystems, https://doi.org/10.1002/2016GC006793, http://doi.wiley.com/10.1002/2016GC006793, 2017.

Mitchell, T. M. and Faulkner, D. R.: The nature and origin of off-fault damage surrounding strike-slip fault zones with a wide range of displacements: A field study from the Atacama fault system, northern Chile, Journal of Structural Geology, 31, 802–816, https://doi.org/10.1016/j.jsg.2009.05.002, http://dx.doi.org/10.1016/j.jsg.2009.05.002, 2009.

Moore, D. E. and Byerlee, J.: Geometry of Recently Active Breaks Along the San Andreas Fault , California, Tech. rep., United States Department of the Interior - Geological Survey, https://doi.org/10.3133/ofr89347, https://pdfs.semanticscholar.org/12f6/e2f32ff93e072e52c0ca6437e4b3af86d242.pdf?{_}ga=2.182238311.1554510574.1573043059-1587575716.1565875639, 1989.

Moore, D. E. and Byerlee, J.: Relationships between sliding behavior and internal geometry of laboratory fault zones and some creeping and locked strike-slip faults of California, Tectonophysics, 211, 305–316, https://doi.org/10.1016/0040-1951(92)90067-G, 1992.

Moore, D. E. and Byerlee, J. D.: Comparative geometry of the San Andreas Fault, California, and laboratory fault zones, Geological Society of America Bulletin, 103, 762–774, https://doi.org/10.1130/0016-7606(1991)103<0762:CGOTSA>2.3.CO;2, 1991.

Moore, D. E., Summers, R., and Byerlee, J. D.: Sliding behavior and deformation textures of heated illite gouge, Journal of Structural Geology, 11, 329–342, https://doi.org/10.1016/0191-8141(89)90072-2, 1989.

Mutlu, O. and Pollard, D. D.: On the patterns of wing cracks along an outcrop scale flaw: A numerical modeling approach using complementarity, Journal of Geophysical Research: Solid Earth, 113, 1–20, https://doi.org/10.1029/2007JB005284, 2008.

Norris, R. J. and Toy, V. G.: Continental transforms: A view from the Alpine Fault, Journal of Structural Geology, 64, 3–31, https://doi.org/10.1016/j.jsg.2014.03.003, http://dx.doi.org/10.1016/j.jsg.2014.03.003, 2014.

Nur, A., Ron, H., and Scottti, O.: Kinematics and Mechanics of Tectonic Block Rotations, Geophysical, 49, 31–46, 1989.

Okubo, K., Bhat, H. S., Rougier, E., Marty, S., Schubnel, A., Lei, Z., Knight, E. E., and Klinger, Y.: Dynamics, radiation and overall energy budget of earthquake rupture with coseismic off-fault damage, Journal of Geophysical Research: Solid Earth, 124, 11 771–11 801, https://doi.org/10.1029/2019jb017304, 2019.

Paola, N. D., Holdsworth, R. E., Viti, C., Collettini, C., and Bullock, R.: Can grain size sensitive flow lubricate faults during the initial stages of earthquake propagation?, Earth and Planetary Science Letters, 431, 48–58, https://doi.org/10.1016/j.epsl.2015.09.002, http://dx.doi.org/10.1016/j.epsl.2015.09.002, 2015.

Peacock, D. C. and Sanderson, D. J.: Effects of layering and anisotropy on fault geometry, Journal of the Geological Society, 149, 793–802, https://doi.org/10.1144/gsjgs.149.5.0793, 1992.

Perrin, C., Manighetti, I., Ampuero, J.-P., Cappa, F., and Gaudemer, Y.: Location of largest earthquake slip and fast rupture controlled by along-strike change in fault structural maturity due to fault growth, Journal of Geophysical Research: Solid Earth RESEARCH, 2, 1–16, https://doi.org/10.1002/2012JB010016.1., 2016a.

Perrin, C., Manighetti, I., and Gaudemer, Y.: Off-fault tip splay networks: A genetic and generic property of faults indicative of their long-term propagation, Comptes Rendus - Geoscience, 348, 52–60, https://doi.org/10.1016/j.crte.2015.05.002, 2016b.

Plesch, A., Nicholson, C., Shaw, J., Marshall, S., Su, M.-H., and Maechling, P.: The SCEC Community Fault Model (CFM), https://www.scec.org/research/cfm, 2017.

Poliakov, A. N. B., Dmowska, R., and Rice, J. R.: Dynamic shear rupture interactions with fault bends and off-axis secondary faulting, Journal of Geophysical Research: Solid Earth, 107, ESE 6–1–ESE 6–18, https://doi.org/10.1029/2001JB000572, http://doi.wiley.com/10.1029/2001JB000572, 2002.

Pozzi, G., Paola, N. D., Nielsen, S. B., Holdsworth, R. E., and Bowen, L.: A new interpretation for the nature and significance of mirror-like surfaces in experimental carbonate-hosted seismic faults, Geology, 46, 583–586, 2018.

Preuss, S., Herrendörfer, R., Gerya, T. V., Ampuero, J., and Dinther, Y.: Seismic and Aseismic Fault Growth Lead to Different Fault Orientations, Journal of Geophysical Research: Solid Earth, 124, 8867–8889, https://doi.org/10.1029/2019jb017324, 2019.

Preuss, S., Jean-Paul Ampuero, Gerya, T. V., and van Dinther, Y.: Model data sets and videos to "Characteristics of earthquake ruptures and dynamic off-fault deformation on propagating faults", ETH Zurich Research Collection, https://doi.org/10.3929/ethz-b-000397242, https://www.research-collection.ethz.ch/handle/20.500.11850/397242, 2020.

Price, R. J. and Kelly, A.: Deformation of age-hardened aluminium alloy crystals II. Fracture, Acta Metallurgica, 12, 979–992, https://doi.org/https://doi.org/10.1016/0001-6160(64)90070-7, 1964.

Rawling, G. C., Baud, P., and Wong, T.-f.: Dilatancy, brittle strength, and anisotropy of foliated rocks: Experimental deformation and micromechanical modeling, Journal of Geophysical Research: Solid Earth, 107, ETG 8–1–ETG 8–14, https://doi.org/10.1029/2001jb000472, 2002.

Rice, J. R.: The mechanics of earthquake rupture, Physics of the Earth's Interior, Amsterdam, North-Holland, 78 edn., https://doi.org/10.1.1.161.3251, http://citeseerx.ist.psu.edu/viewdoc/summary?doi=10.1.1.161.3251, 1980.

Rice, J. R.: Heating , weakening and shear localization in earthquake rupture Subject Areas : Author for correspondence :, Philosophical Transactions of the Royal Society A: Mathematical, Physical and Engineering Sciences, 375, https://doi.org/http://dx.doi.org/10.1098/rsta.2016.0015, 2017.

Rice, J. R., Sammis, C. G., and Parsons, R.: Off-fault secondary failure induced by a dynamic slip pulse, Bulletin of the Seismological Society of America, 95, 109–134, https://doi.org/10.1785/0120030166, 2005.

Riedel, W.: Zur Mechanik geologischer Brucherscheinungen, Centralbl. Mineral. Geol. u. Pal., 1929B, 354–368, 1929.

Ritter, M. C., Rosenau, M., and Oncken, O.: Growing Faults in the Lab: Insights Into the Scale Dependence of the Fault Zone Evolution Process, Tectonics, 37, 140–153, https://doi.org/10.1002/2017TC004787, 2018a.

Ritter, M. C., Santimano, T., Rosenau, M., Leever, K., and Oncken, O.: Sandbox rheometry: Co-evolution of stress and strain in Riedel- and Critical Wedge- experiments, Tectonophysics, 722, 400–409, https://doi.org/10.1016/j.tecto.2017.11.018, https://doi.org/10.1016/j.tecto.2017.11.018, 2018b.

Rubin, A. M. and Ampuero, J. P.: Earthquake nucleation on (aging) rate and state faults, Journal of Geophysical Research: Solid Earth, 110, 1–24, https://doi.org/10.1029/2005JB003686, 2005.

Savage, H. M. and Brodsky, E. E.: Collateral damage: Evolution with displacement of fracture distribution and secondary fault strands in fault damage zones, Journal of Geophysical Research: Solid Earth, 116, https://doi.org/10.1029/2010JB007665, 2011.

Savage, H. M. and Cooke, M. L.: Unlocking the effects of friction on fault damage zones, Journal of Structural Geology, 32, 1732–1741, https://doi.org/10.1016/j.jsg.2009.08.014, http://dx.doi.org/10.1016/j.jsg.2009.08.014, 2010.

Scholz, C. H., Dawers, N. H., Yu, J.-Z., Anders, M. H., and Cowie, P. A.: Fault growth and fault scaling laws: Preliminary results, Journal of Geophysical Research: Solid Earth, 98, 21 951–21 961, https://doi.org/10.1029/93JB01008, http://doi.wiley.com/10.1029/93JB01008, 1993.

Scholz, C. H., Ando, R., and Shaw, B. E.: The mechanics of first order splay faulting: The strike-slip case, Journal of Structural Geology, 32, 118–126, https://doi.org/10.1016/j.jsg.2009.10.007, http://dx.doi.org/10.1016/j.jsg.2009.10.007, 2010.

Scuderi, M. M., Niemeijer, A. R., Collettini, C., and Marone, C.: Frictional properties and slip stability of active faults within carbonate, evaporite sequences: The role of dolomite and anhydrite, Earth and Planetary Science Letters, 369-370, 220–232, https://doi.org/10.1016/j.epsl.2013.03.024, http://dx.doi.org/10.1016/j.epsl.2013.03.024, 2013.

Scuderi, M. M., Collettini, C., Viti, C., Tinti, E., and Marone, C.: Evolution of shear fabric in granular fault gouge from stable sliding to stick slip and implications for fault slip mode, Geology, 45, 731–734, https://doi.org/10.1130/G39033.1, 2017.

Segall, P. and Rice, J. R.: Dilatancy, compaction, and slip instability of a fluid-infiltrated fault, Nature, 100, 155–171, https://doi.org/10.1029/95JB02403, 1995.

Sengör, A., Tüysüz, O., Imren, C., Sakinç, M., Eyidogan, H., Görür, N., Le Pichon, X., and Rangin, C.: The North Anatolian Fault: A New Look, Annual Review of Earth and Planetary Sciences, 33, 37–112, https://doi.org/10.1146/annurev.earth.32.101802.120415, 2004.

Shipton, Z. K., Evans, J. P., Abercrombie, R. E., and Brodsky, E. E.: The Missing Sinks: Slip Localization in Faults, Damage Zones, and the Seismic Energy Budget, in: Earthquakes: Radiated Energy and the Physics of Faulting, Volume 170, edited by Abercrombie, R., McGarr, A., Toro, G. D., and Kanamori, H., Geophysical Monograph Series, https://doi.org/https://doi.org/10.1029/170GM22, 2006.

Sibson, R. H.: Fault rocks and fault mechanisms, Journal of the Geological Society, 133, 191–213, https://doi.org/https://doi.org/10.1144/gsjgs.133.3.0191, 1977.

Sibson, R. H.: Continental fault structure and the shallow earthquake source, Journal of the Geological Society, 140, 741–767, https://doi.org/10.1144/gsjgs.140.5.0741, 1983.

Sibson, R. H.: Thickness of the Seismic Slip Zone, Bulletin of the Seismological Society of America, 93, 1169–1178, https://doi.org/https://doi.org/10.1785/0120020061, 2003.

Sleep, N. H.: Ductile creep, compaction, and rate and state dependent friction within major fault zones, Journal of Geophysical Research: Solid Earth, 100, 13 065–13 080, https://doi.org/10.1029/94jb03340, 1995.

Smith, S. A. F., Billi, A., Di Toro, G., and Spiess, R.: Principal Slip Zones in Limestone : Microstructural Characterization and Implications for the Seismic Cycle (Tre Monti Fault, Central Apennines, Italy), Pure and Applied Geophysics, 168, 2365–2393, https://doi.org/10.1007/s00024-011-0267-5, 2011.

Smith, S. A. F., Nielsen, S., and Toro, G. D.: Strain localization and the onset of dynamic weakening in calcite fault gouge, Earth and Planetary Science Letters, 413, 25–36, https://doi.org/10.1016/j.epsl.2014.12.043, http://dx.doi.org/10.1016/j.epsl.2014.12.043, 2015.

Swanson, M. T.: Fault structure, wear mechanisms and rupture processes in pseudotachylyte generation, Tectonophysics, 204, 223–242, https://doi.org/https://doi.org/10.1016/0040-1951(92)90309-T, 1992.

Swanson, M. T.: Late Paleozoic strike-slip faults and related vein arrays of Cape Elizabeth, Maine, Journal of Structural Geology, 28, 456–473, https://doi.org/10.1016/j.jsg.2005.12.009, 2006.

Tchalenko, J. S.: Similarities between Shear Zones of Different Magnitudes, Geological Society of America Bulletin, 81, 1625–1640, https://doi.org/10.1130/0016-7606(1970)81[1625:SBSZOD]2.0.CO;2, 1970.

Templeton, E. L. and Rice, J. R.: Off-fault plasticity and earthquake rupture dynamics: 1. Dry materials or neglect of fluid pressure changes, Journal of Geophysical Research: Solid Earth, 113, 1–19, https://doi.org/10.1029/2007JB005529, 2008.

Toro, G. D., Goldsby, D. L., and Tullis, T. E.: Friction falls towards zero in quartz rock as slip velocity approaches seismic rates, Nature, 427, 436–439, https://doi.org/https://doi.org/10.1038/nature02249, 2004.

van Dinther, Y., Gerya, T. V., Dalguer, L. A., Corbi, F., Funiciello, F., and Mai, P. M.: The seismic cycle at subduction thrusts: 2. Dynamic implications of geodynamic simulations validated with laboratory models, Journal of Geophysical Research: Solid Earth, 118, 1502–1525, https://doi.org/10.1029/2012JB009479, 2013a.

van Dinther, Y., Gerya, T. V., Dalguer, L. A., Mai, P. M., Morra, G., and Giardini, D.: The seismic cycle at subduction thrusts: Insights from seismo-thermo- mechanical models, Journal of Geophysical Research: Solid Earth, 118, 6183–6202, https://doi.org/10.1002/2013JB010380, 2013b.

van Dinther, Y., Mai, P. M., Dalguer, L. A., and Gerya, T. V.: Modeling the seismic cycle in subduction zones: The role and spatiotemporal occurrence of off-megathrust earthquakes, Geophysical Research Letters, 41, 1194–1201, https://doi.org/10.1002/2013GL058886, 2014.

Vermilye, J. M. and Scholz, C. H.: The process zone: A microstructural view of fault growth, Journal of Geophysical Research, 103, 1998.

Wdowinski, S., Smith-Konter, B., Bock, Y., and Sandwell, D.: Diffuse interseismic deformation across the Pacifi-North America plate boundary, The Geological Society of America, 35, 311–314, https://doi.org/10.1130/G22938A.1, 2007.

Weng, H. and Ampuero, J. P.: The Dynamics of Elongated Earthquake Ruptures, EarthArXiv, https://doi.org/https://doi.org/10.31223/osf.io/9yq8n, 2019.

Willemse, E. J. M. and Pollard, D. D.: On the orientation and patterns of wing cracks and solution surfaces at the tips of a sliding flaw or fault, Journal of Geophysical Research: Solid Earth, 103, 2427–2438, https://doi.org/10.1029/97JB01587, http://doi.wiley.com/10.1029/97JB01587, 1998.

Wollherr, S., Gabriel, A. A., and Mai, P. M.: Landers 1992 "Reloaded": Integrative Dynamic Earthquake Rupture Modeling, Journal of Geophysical Research: Solid Earth, 124, 6666–6702, https://doi.org/10.1029/2018JB016355, 2019.

Woodcock, N. H., Dickson, J. A. D., and Tarasewicz, J. P. T.: Transient permeability and reseal hardening in fault zones: evidence from dilation breccia textures, Geological Society, London, Special Publications, 270, 43–53, https://doi.org/10.1144/gsl.sp.2007.270.01.03, 2007.

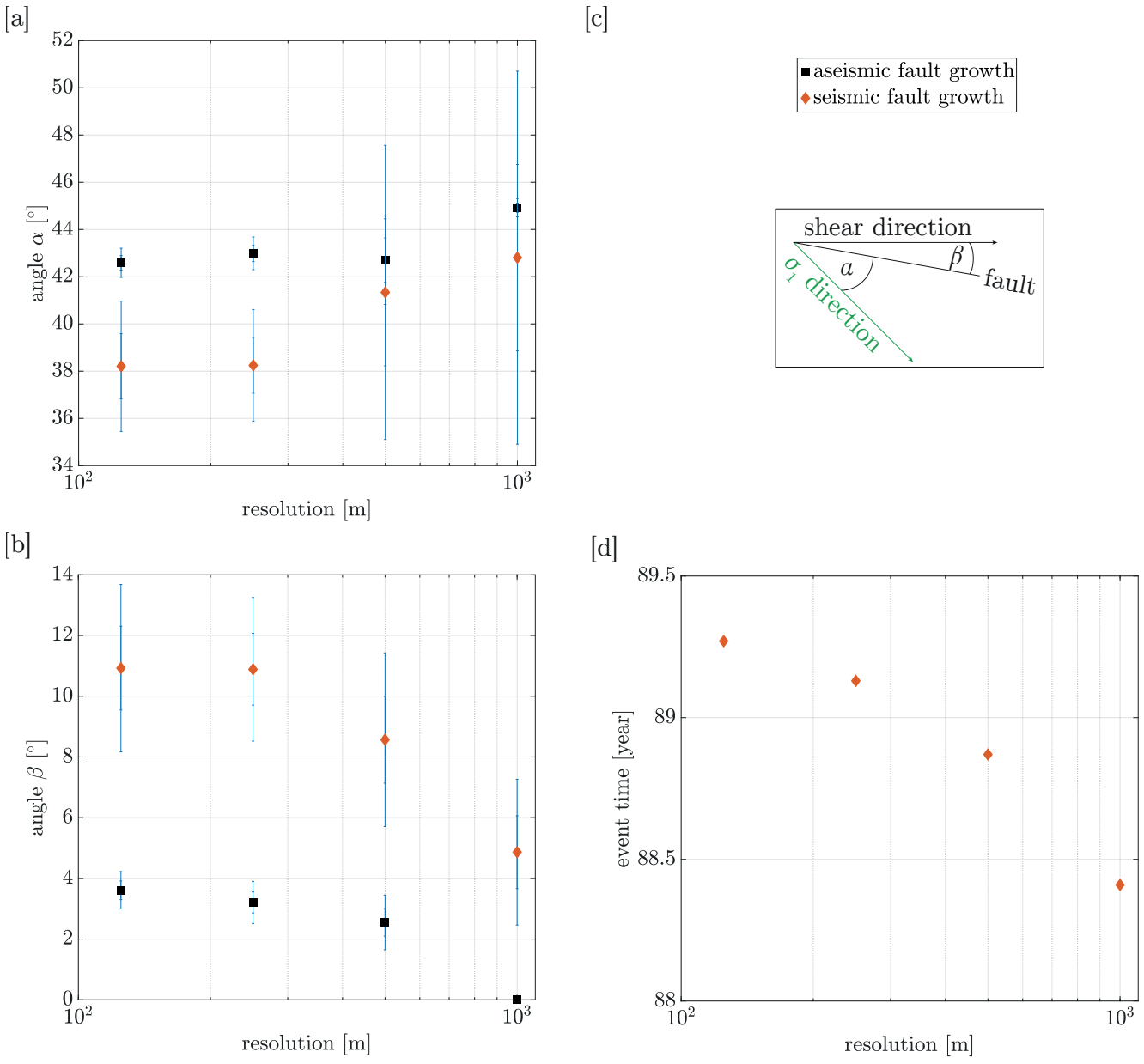

Figure A1. Convergence analysis of fault angle and earthquake time as relation between grid resolution and fault angles and grid resolution and earthquake time start, respectively. Analysis is showing that all seismic and aseismic fault angles as well as earthquake timing converge with grid size. Color-filled symbols indicate different faulting stages. Blue errorbars correspond to errors in measuring the absolute angle β and to spatial variations of the σ_1-direction at the fault tip (details are explained in Preuss et al. (2019)). The solid line corresponds to the standard deviation [-1σ,1σ], the dashed line to the standard deviation [-2σ,2σ]. [a]: Grid resolution in meter versus relative fault angle $\alpha = \sigma_1 - \beta$ (see schematic illustration in [c]). [b]: Grid resolution in meter versus absolute fault angle β. [c]: Fault angle legend and schematic illustration of fault angles. [d]: Grid resolution in meter versus temporal onset of the earthquake in years.